The Astrophysical Journal Supplement Series, 226:7 (20pp), 2016 September doi:10.3847/0067-0049/226/1/7

197 CANDIDATES AND 104 VALIDATED PLANETS IN *K2*'s FIRST FIVE FIELDS

Ian J. M. Crossfield[1,28,30], David R. Ciardi[2], Erik A. Petigura[3,31], Evan Sinukoff[4,32], Joshua E. Schlieder[2,5,33], Andrew W. Howard[4], Charles A. Beichman[2], Howard Isaacson[6], Courtney D. Dressing[3,30], Jessie L. Christiansen[2], Benjamin J. Fulton[4,34], Sébastien Lépine[7], Lauren Weiss[6], Lea Hirsch[6], John Livingston[8], Christoph Baranec[9], Nicholas M. Law[10], Reed Riddle[11], Carl Ziegler[10], Steve B. Howell[5], Elliott Horch[12], Mark Everett[13], Johanna Teske[14], Arturo O. Martinez[7,15], Christian Obermeier[16], Björn Benneke[3], Nic Scott[17], Niall Deacon[18], Kimberly M. Aller[4], Brad M. S. Hansen[19], Luigi Mancini[16], Simona Ciceri[16,20], Rafael Brahm[21,22], Andrés Jordán[21,22], Heather A. Knutson[3], Thomas Henning[16], Michaël Bonnefoy[23,24], Michael C. Liu[4], Justin R. Crepp[25], Joshua Lothringer[1], Phil Hinz[26], Vanessa Bailey[26,27], Andrew Skemer[26,28], and Denis Defrere[23,24,29]

[1] Lunar & Planetary Laboratory, University of Arizona, 1629 E. University Boulevard., Tucson, AZ, USA
[2] NASA Exoplanet Science Institute, California Institute of Technology, Pasadena, CA, USA
[3] Geological and Planetary Sciences, California Institute of Technology, Pasadena, CA, USA
[4] Institute for Astronomy, University of Hawai'i at Mānoa, Honolulu, HI, USA
[5] NASA Ames Research Center, Moffett Field, CA, USA
[6] Astronomy Department, University of California, Berkeley, CA, USA
[7] Department of Physics and Astronomy, Georgia State University, GA, USA
[8] Department of Astronomy, The University of Tokyo, 7-3-1 Bunkyo-ku, Tokyo 113-0033, Japan
[9] Institute for Astronomy, University of Hawai'i at Mānoa, Hilo, HI, USA
[10] Department of Physics and Astronomy, University of North Carolina at Chapel Hill, Chapel Hill, NC, USA
[11] Division of Physics, Mathematics, and Astronomy, California Institute of Technology, Pasadena, CA, USA
[12] Department of Physics, Southern Connecticut State University, New Haven, CT, USA
[13] National Optical Astronomy Observatory, Tucson, AZ, USA
[14] Carnegie Department of Terrestrial Magnetism, Washington, DC, USA
[15] Department of Astronomy, San Diego State University, San Diego, CA, USA
[16] Max Planck Institut für Astronomie, Heidelberg, Germany
[17] Sydney Institute of Astronomy, The University of Sydney, Redfern, Australia
[18] Centre for Astrophysics Research, University of Hertfordshire, UK
[19] Department of Physics & Astronomy and Institute of Geophysics & Planetary Physics, University of California Los Angeles, Los Angeles, CA, USA
[20] Department of Astronomy, Stockholm University, SE-106 91 Stockholm, Sweden
[21] Millennium Institute of Astrophysics, Av. Vicuña Mackenna 4860, 7820436 Macul, Santiago, Chile
[22] Instituto de Astrofísica, Facultad de Física, Pontificia Universidad Católica de Chile, Av. Vicuña Mackenna 4860, 7820436 Macul, Santiago, Chile
[23] Univ. Grenoble Alpes, IPAG, F-38000, Grenoble, France
[24] CNRS, IPAG, F-38000, Grenoble, France
[25] Department of Physics, University of Notre Dame, 225 Nieuwland Science Hall, Notre Dame, IN, USA
[26] Steward Observatory, The University of Arizona, Tucson, AZ, USA
[27] Kavli Institute for Particle Astrophysics and Cosmology, Stanford University, Stanford, CA, USA
[28] Department of Astronomy, University of California, Santa Cruz, Santa Cruz, CA, USA
[29] Departement d'Astrophysique, Geophysique et Oceanographie, Universite de Liege, B-4000 Sart Tilman, Belgium
Received 2016 April 1; revised 2016 June 20; accepted 2016 June 20; published 2016 September 2

ABSTRACT

We present 197 planet candidates discovered using data from the first year of the NASA *K2* mission (Campaigns 0–4), along with the results of an intensive program of photometric analyses, stellar spectroscopy, high-resolution imaging, and statistical validation. We distill these candidates into sets of 104 validated planets (57 in multi-planet systems), 30 false positives, and 63 remaining candidates. Our validated systems span a range of properties, with median values of $R_P = 2.3\ R_\oplus$, $P = 8.6$ days, $T_{\rm eff} = 5300$ K, and $Kp = 12.7$ mag. Stellar spectroscopy provides precise stellar and planetary parameters for most of these systems. We show that *K2* has increased by 30% the number of small planets known to orbit moderately bright stars (1–4 $R_\oplus$, $Kp = 9$–13 mag). Of particular interest are 76 planets smaller than 2 $R_\oplus$, 15 orbiting stars brighter than $Kp = 11.5$ mag, 5 receiving Earth-like irradiation levels, and several multi-planet systems—including 4 planets orbiting the M dwarf K2–72 near mean-motion resonances. By quantifying the likelihood that each candidate is a planet we demonstrate that our candidate sample has an overall false positive rate of 15%–30%, with rates substantially lower for small candidates ($<2R_\oplus$) and larger for candidates with radii $>8R_\oplus$ and/or with $P < 3$ days. Extrapolation of the current planetary yield suggests that *K2* will discover between 500 and 1000 planets in its planned four-year mission, assuming sufficient follow-up resources are available. Efficient observing and analysis, together with an organized and coherent follow-up strategy, are essential for maximizing the efficacy of planet-validation efforts for *K2*, *TESS*, and future large-scale surveys.

[30] NASA Sagan Fellow.
[31] Hubble Fellow.
[32] NSERC Postgraduate Research Fellow.
[33] NASA Postdoctoral Program Fellow.
[34] NSF Graduate Research Fellow.

Key words: catalogs – planets and satellites: fundamental parameters – planets and satellites: general – techniques: high angular resolution – techniques: photometric – techniques: spectroscopic

Supporting material: machine-readable tables

1. INTRODUCTION

Planets that transit their host stars offer unique opportunities to characterize planetary masses, radii, and densities; atmospheric composition, circulation, and chemistry; dynamical interactions in multi-planet systems; and orbital alignments and evolution, to name just a few aspects of interest. Transiting planets are also the most common type of exoplanet known, thanks in large part to NASA's *Kepler* spacecraft. Data from *Kepler*'s initial four-year survey revealed over 4000 candidate exoplanets and many confirmed and validated planets[35] (e.g., Coughlin et al. 2016; Morton et al. 2016). A majority of all exoplanets known today were discovered by *Kepler*. After the spacecraft's loss of a second reaction wheel in 2014, the mission was renamed *K2* and embarked on a new survey of the ecliptic plane, divided into campaigns of roughly 80 days each (Howell et al. 2014). In terms of survey area, temporal coverage, and data release strategy, *K2* provides a natural transition from *Kepler* to the *TESS* mission (Ricker et al. 2014). *Kepler* observed 1/400th of the sky for four years (initially with a default proprietary period), while *TESS* will observe nearly the entire sky for $\geqslant$27 days,[36] with no default proprietary period.

In its brief history *K2* has already made many new discoveries. The mission's data have helped to reveal oscillations in variable stars (Angus et al. 2016) and discovered eclipsing binaries (LaCourse et al. 2015; Armstrong et al. 2016; David et al. 2016a), supernovae (Zenteno et al. 2015), large numbers of planet candidates (Foreman-Mackey et al. 2015; Adams et al. 2016; Vanderburg et al. 2016), and a growing sample of validated and/or confirmed planets (e.g., Vanderburg & Johnson 2014; Crossfield et al. 2015; Huang et al. 2015; Montet et al. 2015; Sanchis-Ojeda et al. 2015; Sinukoff et al. 2016). Here, we report our identification and follow-up observations of 197 candidate planets using *K2* data. Using all available observations and a robust statistical framework, we validate 104 of these as true, bona fide planets, and for the remaining systems we discriminate between obvious false positives and a remaining subset of plausible candidates suitable for further follow-up.

In Section 2 we review our target sample, photometry and transit search, and initial target vetting. Section 3 describes our supporting ground-based observations (stellar spectroscopy and high-resolution imaging; HRI), while Section 4 describes our derivation of stellar parameters. These are followed by our intensive transit light curve analysis in Section 5, the assessment of FPPs for our candidates in Section 6, and a discussion of the results, interesting trends, and noteworthy individual systems in Section 7. Finally, we conclude and summarize in Section 8.

[35] We distinguish "confirmed" systems (with measured masses) from "validated" systems (whose planetary nature has been statistically demonstrated, e.g., with false positive probability (FPP) <1%).

[36] Smaller fractions of the sky will be observed for up to 351 days.

2. K2 TARGETS AND PHOTOMETRY

2.1. Target Selection

In the analysis that follows we use data from all *K2* targets (not just those in our own General Observer proposals[37]). Huber et al. (2016) present the full distribution of stellar types observed by *K2*. For completeness we describe here our target selection strategy, which has successfully proposed for thousands of FGK and M dwarfs through two parallel efforts.

We select our FGK stellar sample from the all-sky *TESS* Dwarf Catalog (TDC; Stassun et al. 2014). The TDC consists of 3 million F5–M5 candidate stars selected from 2MASS and cross-matched with the NOMAD, Tycho-2, *Hipparcos*, APASS, and UCAC4 catalogs to obtain photometric colors, proper motions, and parallaxes. We remove giant stars based on reduced proper motion versus $J-H$ color (see Collier Cameron et al. 2007), and generate a magnitude-limited dwarf star sample from the merged TDC/EPIC by requiring $Kp < 14$ mag for these FGK stars. We impose an anti-crowding criterion and remove all targets with a second star in EPIC (complete down to $Kp \sim 19$ mag; Huber et al. 2016) within 4 arcsec (approximately the *Kepler* pixel size). This last criterion removes <1% of the FGK stars in our proposed samples, improves catalog reliability by reducing false positives, and simplifies subsequent vetting and Doppler follow-up.

We draw our late-type (K and M dwarf) stellar sample primarily from the SUPERBLINK proper motion database (SB, Lépine & Shara 2005) and the PanSTARRS-1 survey (PS1, Kaiser 2002). We use a combination of reduced proper motion, optical/NIR color cuts, and/or SED fitting to capture the majority of M dwarfs (>85%) within 100 pc with little contamination from distant giants. In some *K2* campaigns we supplement our initial database using SDSS, PS1, and/or other photometry to identify additional targets with smaller proper motions (following Aller et al. 2013). We estimate approximate spectral types (SpTs) using tabulated photometric relations (Kraus & Hillenbrand 2007; Pecaut & Mamajek 2013; Rodriguez et al. 2013) and convert SpTs into stellar radii (R_*) based on interferometric studies (Boyajian et al. 2012). Our exact selection criteria for K and M dwarfs have evolved with time, but we typically prioritize this low-temperature stellar sample by requiring a signal-to-noise ratio (S/N) $\gtrsim 8$ for a single transit of an Earth-sized planet, assuming the demonstrated photometric precision of *K2*. We additionally set a magnitude limit of $Kp < 16.5$ mag on this late-type dwarf sample to allow feasible spectroscopic characterization.

2.2. Time-series Photometry

Our team's photometric pipeline (described by, e.g., Crossfield et al. 2015; Petigura et al. 2015 builds on the approach originally outlined by Vanderburg & Johnson (2014). We extract time-series photometry from the target pixel files provided by the project using circular, stationary, soft-edged apertures. During *K2* operations, solar radiation pressure

[37] *K2* Programs 79, 120, 1002, 1036, 2104, 2106, 2107, 3104, 3106, 3107, 4011, 4033.

torques the spacecraft, causing it to roll around the boresight. This motion causes a typical target star to drift across the CCD by ∼1 pixel every ∼6 hr. This motion of stars across the CCD, when combined with inter- and intra-pixel sensitivity variations and aperture losses, results in significant changes in our aperture photometry.

We remove these stellar brightness variations that correlate with spacecraft orientation by first solving for the roll angle between each frame and an arbitrary reference frame using roughly 100 stars of $Kp \sim 12$ mag on an arbitrary output channel. Then, we model the time- and roll-dependent brightness variations using a Gaussian process with a squared-exponential kernel. We apply apertures with radii ranging from 1 to 7 pixels and select the aperture that minimizes the residual noise in the corrected light curve (computed on three-hour timescales). This minimization balances two competing effects: larger apertures yield smaller systematic errors (because aperture losses are smaller), while smaller apertures incur less background noise. All of our processed light curves are available for download at the NExScI ExoFOP website.[38]

2.3. Identifying Transit-like Signals

We search our calibrated photometry for planetary transits using the TERRA algorithm (Petigura et al. 2013a). After running TERRA, we flag stars with putative transits having S/N > 12 as threshold-crossing events (TCEs) for visual inspection. Below this level, transit signals surely persist but TCEs become dominated by spurious detections. Residual outliers in our photometry prevent us from identifying large numbers of candidates at lower S/N. In order to reduce the number of spurious detections we require that TCEs have orbital periods $P \geqslant 1$ days, and that they also show three transits. This last criterion sets an upper bound to the longest period detectable in our survey at half the campaign baseline, or ∼37 days.[39] Thus many longer-period planets likely remain to be found in these data sets, in a manner analogous to the discovery of HIP-116454b in *K2*'s initial engineering run (Vanderburg et al. 2016) and additional single-transit candidates identified in Campaigns 1–3 (Osborn et al. 2016).

In our analysis, each campaign yields roughly 1000 TCEs. The distribution of their orbital periods, shown in Figure 1, reveals discrete peaks at $P = 1.5$, 2, 4, 8, and 16 days. These sharp peaks likely correspond to the 6 hr periodicity of small-scale maneuvering tweaks to rebalance solar pressure and/or to the 48 hr periodicity of *K2*'s reaction wheel momentum dumps (Van Cleve et al. 2016). Both these effects could induce correlated photometric jitter on integer multiples of this timescale. We also see a smoother increase in TCEs toward longer periods ($P \gtrsim 16$ days) that our manual vetting (described below) shows as corresponding to an increasing false positive rate (FPR) for TCEs showing just 3–5 transit-like events.

In each campaign, our manual vetting process begins with these TCEs and results in well-defined lists of astrophysical variables, including robust planet candidates for further follow-up and validation. TERRA produces a set of diagnostics for every TCE with a detection above our S/N limit, which we use to determine whether the event was likely caused by a

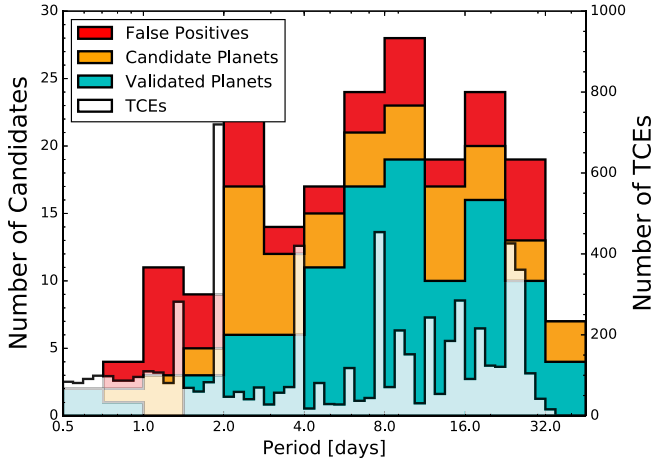

Figure 1. Distribution of orbital periods of transit-like signals identified in our analysis. The pale, narrow-binned histogram (axis at right) indicates the Threshold-Crossing Events (TCEs) identified by TERRA in our initial transit search (see Section 2). The coarser histograms (axis at left) indicate the cumulative distributions of 104 validated planets (blue-green; FPP < 0.01), 30 false positive systems (red; FPP > 0.99), and 63 candidates of indeterminate status (orange).

candidate planet, eclipsing binary, periodic variable, or noise. The diagnostics include a summary of basic fit parameters and a suite of diagnostic plots to visualize the nature of the TCE. These plots include the TERRA periodogram, a normalized phase-folded light curve with a best-fit model, the light curve phased to 180° to look for eclipses or misidentified periods, the most probable secondary eclipse identified at any phase, and an autocorrelation function. When vetting, the user flags each TCE as an object of interest or not, where objects of interest can be either candidate planets, eclipsing binaries, or variable stars. We elevate any TCE showing no obvious warning signs to the status of "planet candidate," i.e., an event that is almost surely astrophysical in nature, possibly a transiting planet, and not obviously a false positive scenario like a background eclipsing binary. We quantify the FPPs of all our candidates in Section 6. Figure 2 shows an example of a TERRA-derived light curve for a typical candidate.

Once we identify a candidate, we re-run TERRA to search for additional planets in that system as described by Sinukoff et al. (2016). In brief, we mask out the photometry associated with transits of the previously identified candidate and run TERRA again to look for additional box-shaped signals. We repeat this process until no candidates are identified with S/N > 8 or the number of candidates exceeds five. We typically find <10 multi-candidate systems per campaign, with a maximum of four planets detected per star.

3. SUPPORTING OBSERVATIONS

3.1. High-resolution Spectroscopy: Observations

3.1.1. Keck/HIRES

We obtained high-resolution optical spectra of 83 planet candidate hosts using the HIRES echelle spectrometer (Vogt 1994) on the 10 m Keck I telescope. These spectra were collected using the standard procedures of the California Planet Search (CPS; Howard et al. 2010). We used the "C2" decker (0.″87 × 14″ slit), which is long enough to simultaneously measure the spectra of the target star and the sky background

[38] https://exofop.ipac.caltech.edu

[39] The handful of candidates with $P > 37$ days were found by visual inspection.

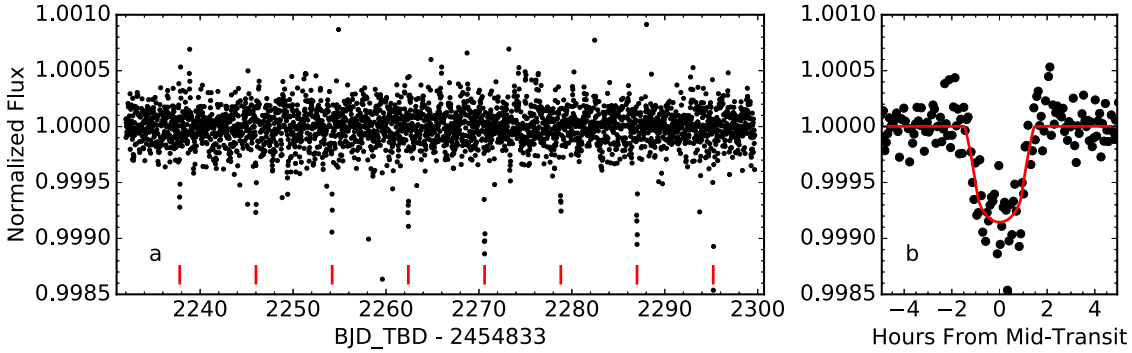

Figure 2. Example light curve of K2-77 (EPIC 210363145), which hosts one validated planet: (a) during all of Campaign 4, with individual transit times indicated, and (b) phase-folded, with the best-fit transit model overplotted in red. The transit parameters for all candidates are listed in Table 8.

with spectral resolution $R = 55{,}000$. The sky was subtracted from each stellar spectrum. We used the HIRES exposure meter to automatically terminate each exposure once the desired S/N was reached, typically after 1–20 minutes. For stars with $V < 13.0$ mag, exposure levels were set to achieve S/N = 45 per pixel at 550 nm. Exposures of fainter stars were terminated at S/N = 32 per pixel—enough to derive stellar parameters while keeping exposure times reasonable. For stars that were part of subsequent Doppler campaigns, we measured additional HIRES spectra with higher S/N. These RV measurements will be the subject of a series of forthcoming papers.

3.1.2. Automated Planet Finder (APF)/Levy

We obtained spectra of 27 candidate host stars using the Levy high-resolution optical spectrograph mounted at the APF. Each spectrum covers a continuous wavelength range from 374 to 970 nm. We observed the stars using either the $2'' \times 8''$ slit for a spectral resolution of $R \approx 80{,}000$, or, to minimize sky contamination, the $1'' \times 3''$ slit for a spectral resolution of $R \approx 100{,}000$. We initially observed all bright targets using the $2'' \times 8''$ slit to maximize S/N but soon noticed that sky contamination was a serious problem on nights with a full or gibbous moon. All APF spectra collected after 2015 May 21 were observed using the $1'' \times 3''$ decker. In all cases, we collected three consecutive exposures and combined the extracted 1D spectra using a sigma-clipped mean to reject cosmic rays. All targets were observed at just a single epoch. The final S/N of the combined spectra ranges from roughly 25 to 50 per pixel.

3.1.3. MPG 2.2 m/FEROS

We obtained spectra of a small number of candidate stellar hosts using the FEROS fiber-fed echelle spectrograph (Kaufer & Pasquini 1998) at the 2.2 m MPG telescope. Each spectrum covers a continuous wavelength range from 350 to 920 nm with an average resolution of $R \sim 48{,}000$. Our FEROS exposure times were chosen according to the brightness of each target and ranged from 10 to 30 minutes. Simultaneously with the science images we acquired spectra of a ThAr lamp for wavelength calibration.

The FEROS data are processed through a dedicated pipeline built from a modular code (CERES, R. Brahm et al. 2016, in preparation) designed to reduce, extract and analyze data from different echelle spectrographs in an automated, homogeneous and robust way. This pipeline is similar to the calibration and optimal extraction approach described by Jordán et al. (2014). We compute a global wavelength solution from the calibration ThAr image by fitting a Chebyshev polynomial as function of the pixel position and echelle order number. The instrumental velocity drifts during the night are computed using the the extracted spectra of the ThAr lamp acquired during the science observations with the reference fiber. The barycentric correction is performed using the JPLephem package. Radial velocities (RVs) and bisector spans are determined by cross-correlating the continuum-normalized stellar spectrum with a binary mask derived from a G2 dwarf's spectrum (for more details see, e.g., Baranne et al. 1979; Queloz 1995). We normalize the stellar continuum to minimize the systematic errors that would be induced in the derived velocity by differences in spectral slope caused by different reddening or stellar type.

3.2. High-resolution Spectroscopy: Methods and Results

As part of our false positive analysis (described in Section 6), we use our high-resolution Keck/HIRES spectra to search for additional spectral lines in the stellar spectra. This method is sensitive to secondary stars that lie within $0\farcs4$ of the primary star (one half of the slit width) and that are as faint as 1% of the apparent brightness of the primary star (Kolbl et al. 2015). The approach therefore complements the AO and speckle imaging described in Section 3.3 (Ciardi et al. 2015; Teske et al. 2015).

The search for secondary lines in the HIRES spectra begins with a match of the primary spectrum to a catalog of nearby, slowly rotating, FGKM stars from the CPS. The best match from the catalog is identified, subtracted from the primary spectrum, and the residuals are then searched (using the same catalog) to identify any fainter second spectrum. This method is insensitive to companion stars with velocity offsets of $\lesssim$10 km s^{-1}, in which cases multiple stellar lines would be blended too closely together. This method is optimized for slowly rotating FGKM stars, so stars earlier than F and those with $v \sin i > 10$ km s^{-1} are more difficult to detect due to their having fewer and/or broader spectral lines. The technique is less sensitive for stars with $T_{\rm eff} \lesssim 3500$ K due to the small number of such stars in the CPS catalog. The derived constraints for all targets are listed in Table 3, and we use them in our false positive analysis described in Section 6. Figure 3 shows an example of a Keck/HIRES spectrum, together with the secondary line search results and derived stellar parameters (see Section 4).

We performed a similar analysis for the subset of stars observed by the FEROS spectrograph. Table 1 lists these stars,

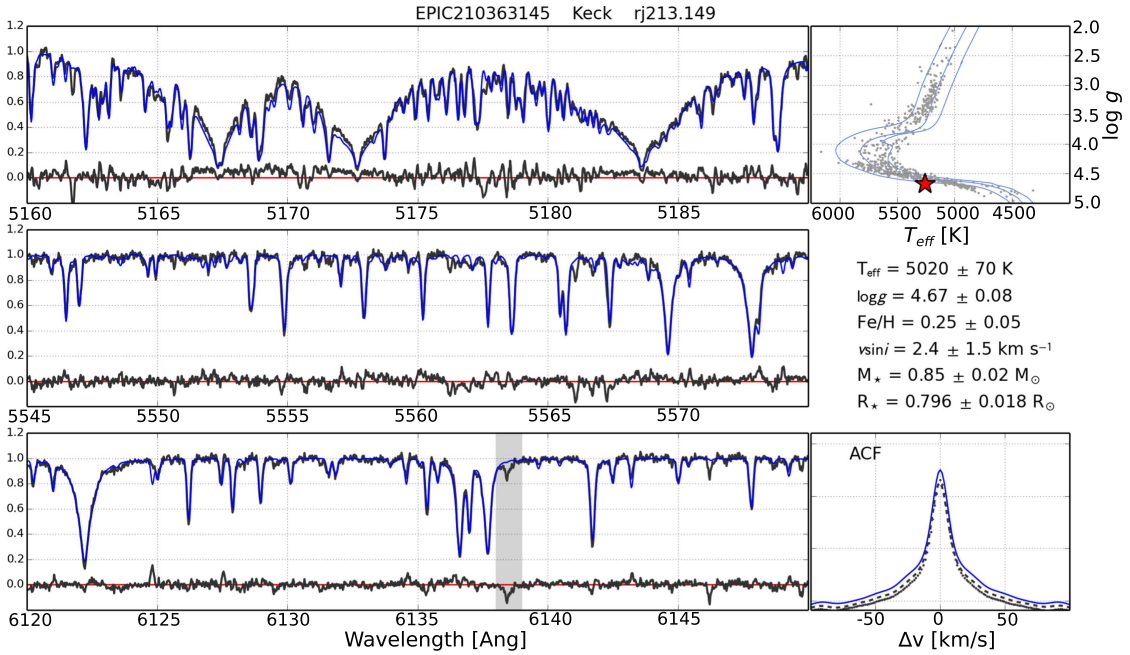

Figure 3. Example Keck/HIRES stellar spectrum (blue), template match (black), and derived parameters for K2-77 (EPIC 210363145). The star has low $v \sin i$, moderate $T_{\rm eff}$, and shows no evidence for additional stellar companions in the spectroscopic autocorrelation function (ACF). The upper-right panel plots the derived stellar parameters against the parameters of the `SpecMatch` template stars. Stellar parameters for all targets are listed in Table 7, and results of ACF analyses are in Table 3.

Table 1
FEROS Follow-up Observations

EPIC	Observation Note
201176672	Multiple peaks in CCF; likely stellar blend.
201270176	Multiple peaks in CCF; likely stellar blend.
202088212	Multiple peaks in CCF; likely stellar blend.
203929178	Multiple peaks in CCF; likely stellar blend.
204873331	Multiple peaks in CCF; likely stellar blend.
203485624	Very broad CCF peak, $v \sin i > 50$ km s^{-1}.
205148699	Single-peaked CCF, phased RV variations of $\pm$28 km s^{-1}.
201626686	Single-peaked CCF, unphased RV jitter of $\pm$ 50 m s^{-1}.
203771098	Single-peaked CCF, RV variations <20 m s^{-1}.
201505350	Single-peaked CCF, ~20 m s^{-1} RV variation between two epochs.
201862715	Single-peaked CCF.

Table 2
False Positive Rates

Category	FP Rate
$R_P \leqslant 2R_\oplus$	0.07
$2 \leqslant R_P/R_\oplus \leqslant 8$	0.08
$R_P \geqslant 8R_\oplus$	0.54
$P \leqslant 3$ days	0.36
$3 \leqslant P \leqslant 15$	0.12
$P \geqslant 15$ days	0.21
Entire Sample	0.20

most of which host candidate hot Jupiters. Three show obvious signs of multiple peaks in the stellar cross-correlation, indicating these sources are blends of multiple stars; a fourth shows an extremely high rotational velocity. As described in Section 6, we find FPPs of >50% for all four of these systems, indicating that most are likely false positives and low-priority targets for future follow-up.

By obtaining FEROS spectra at multiple epochs, we detect RV variations from EPIC 205148699 in phase with the transit signal and with semi-amplitude $K \sim 28$ km s^{-1}, indicating that this system is an eclipsing stellar binary. For EPIC 201626686, 11 RV measurements over 40 days reveal variations at the level of $\pm$50 m s^{-1}. Since these variations are not in phase with the orbital period of the detected transits, we do not consider this system to be a false positive. Finally, multiple RV measurements also set as an upper limit on the RV variations of K2-24 (EPIC 203771098) of <20 m s^{-1} (consistent with the analysis of Petigura et al. 2016). Our analysis in Section 6 ultimately finds FPP < 0.01 for all three of these systems, indicating that these are validated planets.

Single-epoch FEROS observations reveal that both K2-19 (EPIC 201505350) and EPIC 201862715 are single-lined dwarf stars, consistent with our validation of the former (the latter has a close stellar companion that prevents us from validating the system; see Section 6). A second observation of K2-19 taken three days later shows an RV variation of ~20 m s^{-1}, roughly consistent with the RV signal reported by Barros et al. (2015).

3.3. High-resolution Imaging

3.3.1. Observations

We obtained HRI for 164 of our candidate systems. Our primary instrument for this work was NIRC2 at the 10 m Keck II telescope, with which we observed 110 systems. Most were observed in Natural Guide Star (NGS) mode, though we used Laser Guide Star (LGS) mode for a subset of targets orbiting fainter stars. As part of multi-semester program GN-2015B-LP-5 (PI Crossfield) at Gemini Observatory, we observed 40 systems with the NIRI camera (Hodapp 2003) in the K-band using NGS or LGS modes. We also observed 33 stars with PHARO/PALM-3000 (Hayward et al. 2001; Dekany

Table 3
HIRES Follow-up Observations

EPIC	Flag	Note
201295312	1	1%
201338508	1	1%
201367065	1	1%
201384232	1	1%
201393098	1	1%
201403446	1	1%
201445392	1	1%
201465501	1	1%
201505350	1	1%
201546283	1	1%
201549860	1	1%
201577035	1	1%
201613023	1	1%
201629650	1	1%
201647718	1	1%
201677835	1	1%
201702477	1	1%
201713348	1	1%
201736247	1	1%
201754305	1	1%
201828749	1	1%
201912552	1	1%
201920032	1	1%
202071401	1	1%
202083828	1	1%
202089657	1	1%
202675839	1	1%
203771098	1	1%
203826436	1	1%
204129699	1	1%
204221263	1	1%
204890128	1	1%
205071984	1	1%
205570849	1	1%
205916793	1	1%
205924614	1	1%
205944181	1	1%
205999468	1	1%
206011496	1	1%
206011691	1	1%
206024342	1	1%
206026136	1	1%
206026904	1	1%
206036749	1	1%
206038483	1	1%
206044803	1	1%
206061524	1	1%
206096602	1	1%
206101302	1	1%
206125618	1	1%
206144956	1	1%
206153219	1	1%
206154641	1	1%
206155547	1	1%
206159027	1	1%
206181769	1	1%
206192335	1	1%
206245553	1	1%
206247743	1	1%
206268299	1	1%
206348688	1	1%
206432863	1	1%
206439513	1	1%
206495851	1	1%

Table 3
(Continued)

EPIC	Flag	Note
210363145	1	1%
210389383	1	1%
210400751	1	1%
210402237	1	1%
210403955	1	1%
210414957	1	1%
210448987	1	1%
210483889	1	1%
210484192	1	1%
210508766	1	1%
210577548	1	1%
210609658	1	1%
210666756	1	1%
210707130	1	1%
210718708	1	1%
210731500	1	1%
210754505	1	1%
210894022	1	1%
210957318	1	1%
210968143	1	1%
211089792	1	1%
211099781	1	1%
211152484	1	1%
201637175	2	N/A; star too cool
203710387	2	N/A; star too cool
202126852	3	N/A; high $v \sin i$
202126888	3	N/A; high $v \sin i$
205703094	3	N/A; Vsini too high
208833261	3	N/A; high $v \sin i$
210954046	3	N/A; high $v \sin i$
210958990	3	N/A; high $v \sin i$
211147528	3	N/A; high $v \sin i$
206027655	4	Marginal detection of 5% binary at -10 km s^{-1}.
206028176	4	Marginal detection at 10 km s^{-1} separation
201324549	5	triple star system; ~20% brightness
202088212	5	companion; 3–13% as bright as primary; 25 km s^{-1}.
203753577	5	15% companion at 16 km s^{-1} separation
205947161	5	Nearly equal flux binary
206135267	5	Obvious Binary; 50% flux of primary
206267115	5	SB2; near equal at 80 km s^{-1}
206543223	5	SB2; 23% flux of primary
209036259	5	Obvious triple system.
210401157	5	Strange, composite spectrum.
210513446	5	SB2; 2% companion at del-RV = 122 km s^{-1}
210558622	5	SB2; 3% companion at del-RV = 119 km s^{-1}
210744674	5	SB2; equal flux secondary
210789323	5	SB2; 22% companion at del-RV = -83 km s^{-1}
210903662	5	SB2; near equal binary

Notes.
[1] No detection of second spectrum at noted flux ratio.
[2] Star is unfit for ReaMatch: $T_{\rm eff}$ below 3500 K.
[3] Star is unfit for ReaMatch: $v \sin i$ above 10 km s^{-1}.
[4] Ambiguous detection.
[5] Obvious detection.

(This table is available in machine-readable form.)

et al. 2013) at the 5 m Hale Telescope and 14 systems with LMIRCam at LBT (Leisenring et al. 2012), all at the *K*-band. We observed 39 stars at visible wavelengths using the automated Robo-AO laser adaptive optics system at the Palomar 1.5 m telescope (Baranec et al. 2013, 2014). These

Table 4
FEROS Radial Velocities

EPIC	BJD	RV	σ_{RV}	$t_{\rm int}$	S/N
203294831	2457182.56854355	6.235	0.093	600	45
203771098	2457182.57744262	0.713	0.010	600	82
201176672	2457182.58920619	41.702	0.029	1800	25
201626686	2457182.62251241	49.133	0.015	600	49
203929178	2457182.67319105	−130.200	0.221	600	54
203771098	2457183.50141524	0.725	0.010	600	78
203929178	2457183.53736243	64.251	0.276	600	51
201626686	2457183.54133676	49.090	0.011	600	76
204873331	2457183.74219492	48.694	0.620	900	46
203485624	2457183.75453967	93.324	1.867	900	47
203294831	2457183.76528655	7.172	0.076	600	46
205148699	2457183.77680036	−41.853	0.058	900	43
203294831	2457184.51873516	6.106	0.118	600	34
204873331	2457184.54186421	−39.425	0.559	900	43
205148699	2457184.55524152	−32.892	0.055	900	46
203771098	2457184.57256456	0.707	0.010	600	90
203929178	2457184.58722675	−80.916	0.226	600	57
203485624	2457184.70016264	−8.811	1.983	900	54
201176672	2457185.53558417	41.739	0.023	1800	31
201626686	2457185.55294623	49.105	0.011	600	74
203294831	2457185.61605114	6.799	0.076	600	43
203929178	2457185.67144651	−3.928	0.841	600	53
205148699	2457185.68276227	−61.542	0.055	900	45
204873331	2457185.76186667	−51.492	0.320	900	53
203485624	2457185.77667465	−58.772	3.136	900	39
203485624	2457186.59017442	−20.641	1.277	900	40
205148699	2457186.60319043	−77.486	0.068	900	35
205148699	2457186.61615822	−77.408	0.060	900	41
204873331	2457186.62889121	6.458	0.327	900	35
203929178	2457186.68052468	−20.963	0.161	600	44
203294831	2457186.80984085	5.598	0.121	600	37
203929178	2457187.61615918	−76.018	0.467	600	59
203485624	2457187.62722491	−121.651	2.046	900	52
201626686	2457190.49169087	49.070	0.010	600	80
203485624	2457190.57993074	−17.006	1.498	900	58
203294831	2457190.59359013	5.611	0.072	600	61
203294831	2457191.51831070	5.522	0.083	600	50
203485624	2457191.53066007	69.097	1.920	900	3
203929178	2457191.54262838	−88.136	0.276	600	53
204873331	2457191.55366638	42.413	0.630	900	36
201176672	2457192.52186285	41.755	0.026	1800	26
201626686	2457192.54283939	49.094	0.015	600	46
203294831	2457192.56384913	1.127	0.770	600	21
201626686	2457193.51718740	49.149	0.015	600	49
203294831	2457193.53338541	5.362	0.113	600	36
203485624	2457193.54441500	−62.799	1.150	900	35
204873331	2457193.56058533	−39.060	0.228	900	62
205148699	2457193.57490799	−38.108	0.048	900	54
203929178	2457193.74554128	−27.479	0.915	600	62
201176672	2457194.51197780	41.713	0.022	1800	32
201626686	2457194.52827067	49.060	0.011	600	73
203929178	2457194.54604512	−78.496	0.263	600	63
203485624	2457194.57421092	40.485	2.366	900	40
203294831	2457194.58577034	2.920	0.183	600	50
203771098	2457194.59578556	0.720	0.010	600	97
205148699	2457194.60718775	−65.417	0.047	900	55
204873331	2457194.76473872	−30.284	0.301	900	42
203485624	2457195.57768234	−30.056	3.353	900	43
203929178	2457195.59152469	62.791	0.432	600	40
204873331	2457195.60248537	51.545	0.467	900	41
205148699	2457195.61518621	−78.246	0.073	900	33
203294831	2457195.67227197	2.509	0.482	600	21
203771098	2457195.68202812	0.683	0.015	600	32
203294831	2457211.65688105	4.917	0.081	600	43

Table 4
(Continued)

EPIC	BJD	RV	σ_{RV}	$t_{\rm int}$	S/N
203929178	2457211.67035362	74.751	0.344	600	55
203771098	2457211.68015495	0.722	0.010	600	95
203485624	2457211.69331295	42.800	6.707	900	41
204873331	2457211.70909075	0.643	0.274	900	54
205148699	2457211.72234337	−56.025	0.047	900	53
201626686	2457218.47908419	49.071	0.012	900	60
201626686	2457219.46201643	49.100	0.013	600	57
201626686	2457220.48312511	49.054	0.013	600	57
201626686	2457221.48191204	49.087	0.012	600	69
202088212	2457408.67412585	−17.112	0.021	900	87
201505350	2457409.82308403	7.334	0.011	1500	45
201270176	2457410.85912543	91.924	0.088	1100	37
201862715	2457410.87002659	13.448	0.010	420	69
201505350	2457412.79619955	7.369	0.011	1500	47
201862715	2457412.84747439	13.645	0.010	420	75
201270176	2457413.72138662	80.691	0.064	1100	52

(This table is available in machine-readable form.)

data were acquired and reduced separately using the standard Robo-AO procedures outlined by Law et al. (2014).

We acquired the data from all our large-aperture AO observations (NIRC2, NIRI, LMIRCam, PHARO) in a consistent manner. We observed at up to nine dither positions, using integration times short enough to avoid saturation (typically $\leqslant$60 s). We use the dithered images to remove sky background and dark current, and then align, flat-field, and stack the individual images.

Through our Long-Term Gemini program we also acquired high-resolution speckle imaging of 32 systems in narrowband filters centered at 692 and 880 nm using the DSSI camera (Horch et al. 2009, 2012) at the Gemini North telescope. The DSSI observing procedure is typically to center the target star in the field, set up guiding, and take data using 60 ms exposures. The total integration time varies by target brightness and observing conditions. We measure background sensitivity in a series of concentric annuli around the target star. The innermost data point represents the telescope diffraction limit, within which we set our sensitivity to zero. After measuring our sensitivity across the DSSI field of view, we interpolate through the measurements using a cubic spline to produce a smooth sensitivity curve.

3.3.2. Contrast and Stellar Companions

We estimate the sensitivity of all our HRI data by injecting fake sources into the final combined images with separations at integral multiples of the central source's FWHM (see, e.g., Adams et al. 2012; Ziegler et al. 2016). Figure 4 shows an example of a Keck/NIRC2 NGS image and the resulting 5σ contrast curve. The median contrast curves achieved by each HRI instrument are shown in Figure 5 together with all detected stellar companions. The companions are also listed in Table 5. Contrast curves for each individual system are uploaded to the ExoFOP website. In addition, Table 10 includes the total integration times and filters used for all candidates observed in our follow-up efforts.

The contrast curves are plotted in the band of observations, which ranges from optical wavelengths (DSSI; Robo-AO) to the *K*-band (large-aperture AO systems). These in-band

Table 5
HRI-detected Stellar Companions

EPIC	r_{ap} ($''$)	ρ ($''$)	Delta mag (mag)	Filter	Telescope
201176672	11.94	0.340	2.77	K	Keck2
201295312	11.94	8.110	4.00	K	Keck2
201295312	11.94	8.070	4.10	K	Palomar
201324549	11.94	0.090	0.43	K	GemN-NIRI
201488365	⋯	4.100	9.56	i	Robo-AO
201505350	11.94	0.160	0.36	K	Palomar
201546283	7.96	3.030	5.83	i	Robo-AO
201546283	7.96	2.960	3.74	K	Keck2
201626686	11.94	15.390	2.43	K	Palomar
201629650	11.94	3.210	5.79	K	Keck2
201828749	11.94	2.540	1.97	i	Robo-AO
201828749	11.94	2.450	1.07	K	Keck2
201828749	11.94	2.440	1.11	K	Palomar
201862715	11.94	1.450	0.90	i	Robo-AO
201862715	11.94	1.470	0.51	K	Palomar
202059377	11.94	0.390	0.34	i	Robo-AO
202059377	11.94	0.360	0.32	K	LBT
202066212	⋯	9.120	0.43	K	Palomar
202066212	⋯	10.580	2.72	K	Palomar
202066537	7.96	2.280	0.69	i	Robo-AO
202066537	7.96	2.290	0.58	K	LBT
202071289	11.94	0.060	0.09	K	Keck2
202071401	15.92	2.880	2.49	i	Robo-AO
202071401	15.92	6.230	5.05	i	Robo-AO
202071401	15.92	2.840	1.70	K	Keck2
202071401	15.92	2.840	1.79	K	Palomar
202071401	15.92	6.050	5.23	K	Palomar
202071645	11.94	3.700	7.19	i	Robo-AO
202071645	11.94	3.360	7.06	K	Palomar
202071645	11.94	3.630	7.43	K	Palomar
202071645	11.94	9.290	3.67	K	Palomar
202071645	11.94	10.850	5.88	K	Palomar
202083828	11.94	5.530	5.02	i	Robo-AO
202088212	15.92	1.310	6.79	K	Keck2
202089657	15.92	8.550	5.28	K	Palomar
202089657	15.92	9.210	5.58	K	Palomar
202089657	15.92	11.160	4.67	K	Palomar
202089657	15.92	11.630	6.73	K	Palomar
202126849	15.92	4.610	5.70	i	Robo-AO
202126852	15.92	7.150	7.44	K	Palomar
202126852	15.92	3.730	6.99	K	Palomar
202126852	15.92	7.170	7.38	i	Robo-AO
202126887	15.92	5.770	2.79	i	Robo-AO
202126887	15.92	7.260	2.33	i	Robo-AO
202126887	15.92	5.580	2.53	K	Keck2
202126887	15.92	7.200	1.41	K	Keck2
202126888	15.92	6.700	5.98	i	Robo-AO
202565282	7.96	2.170	5.19	K	Keck2
203929178	19.9	0.110	1.37	K	Keck2
204043888	7.96	5.520	4.73	K	Keck2
204489514	15.92	5.390	4.49	K	Keck2
204890128	15.92	7.510	1.55	K	Keck2
205029914	11.94	3.320	0.87	K	Keck2
205064326	11.94	4.270	3.92	K	Keck2
205148699	11.94	0.090	0.83	K	Keck2
205686202	11.94	0.790	3.82	K	Keck2
205703094	11.94	0.140	0.37	K	Keck2
205916793	11.94	7.300	0.35	K	Palomar
205962680	11.94	0.480	0.27	K	Keck2
205999468	7.96	18.500	3.27	K	Palomar
206011496	7.96	0.980	2.81	K	Keck2
206047297	11.94	9.560	5.90	K	Palomar
206061524	7.96	0.410	1.37	K	Palomar
206192335	11.94	2.240	6.18	K	GemN-NIRI
206192335	11.94	2.260	6.21	K	Palomar
207389002	11.94	5.940	2.36	K	GemS-GNIRS
207389002	11.94	5.370	2.96	K	GemS-GNIRS
207389002	11.94	5.910	2.29	i	Robo-AO
207475103	15.92	0.100	0.12	K	LBT
207475103	15.92	4.340	3.18	i	Robo-AO
207475103	15.92	7.610	−2.11	i	Robo-AO
207475103	15.92	7.700	2.51	i	Robo-AO
207517400	15.92	3.530	2.63	i	Robo-AO
207517400	15.92	3.430	1.92	K	Palomar
207517400	15.92	8.320	1.35	K	Palomar
207517400	15.92	10.620	−2.12	K	Palomar
207739861	11.94	5.440	1.62	i	Robo-AO
208445756	11.94	5.970	1.37	i	Robo-AO
208445756	11.94	5.850	1.19	K	Palomar
208445756	11.94	11.290	3.06	K	Palomar
208445756	11.94	13.130	3.79	K	Palomar
208445756	11.94	12.000	4.05	K	Palomar
209036259	15.92	4.000	2.96	i	Robo-AO
210401157	5.572	0.500	2.47	a	GemN-Spk
210401157	5.572	0.490	2.27	b	GemN-Spk
210401157	5.572	0.470	1.67	K	Keck2
210414957	15.92	0.790	2.41	K	GemN-NIRI
210414957	15.92	1.020	4.95	K	GemN-NIRI
210513446	7.96	0.240	1.26	K	GemN-NIRI
210666756	5.572	2.360	1.30	K	GemN-NIRI
210666756	5.572	7.850	1.28	K	GemN-NIRI
210769880	15.92	0.780	5.39	K	GemN-NIRI
210954046	7.96	2.930	1.45	K	GemN-NIRI
210958990	11.94	1.740	2.52	a	GemN-Spk
210958990	11.94	1.790	2.80	b	GemN-Spk
210958990	11.94	1.820	1.71	K	Keck2
211089792	15.92	4.240	0.89	K	GemN-NIRI
211147528	15.92	1.330	6.75	b	GemN-Spk
211147528	15.92	1.300	5.02	K	Keck2
203099398	⋯	1.970	1.67	K	Keck2
203867512	⋯	0.453	0.61	K	Keck2
204057095	⋯	0.790	2.71	K	Keck2
204057095	⋯	0.870	2.97	K	Keck2
204750116	⋯	2.980	5.91	K	Keck2

(This table is available in machine-readable form.)

magnitude differences set upper limits on the maximum amount of blending possible within the *Kepler* bandpass. If the companion has the same color as the primary, then the measured Δmag is indeed the ΔKp. If the companion is redder, then the Kp-band flux ratio is even smaller. All detected sources are included in Table 5, even though some lie outside of our photometric apertures. In these cases the detected companion has little or no impact on the transit parameters and FPPs derived below. We discuss such considerations more thoroughly in Section 6.2.

4. STELLAR PARAMETERS

Stellar parameters are needed to convert the physical properties measured by our transit photometry into useful planetary parameters such as radius (R_P) and incident

Table 6
Disposition of Multi-star Candidates

EPIC	$\rho < 4''$	$F_2/F_1 < \delta'$	Comment
201176672	True	True	Cannot validate candidate.
201295312	False	True	Same depth for $r = 1''$ aperture.
201324549	True	True	Cannot validate candidate.
201546283	True	True	Cannot validate candidate.
201626686	False	True	Shallower transit with $r = 1''$; likely FP.
201629650	True	True	Cannot validate candidate.
201828749	True	True	Cannot validate candidate.
201862715	True	True	Cannot validate candidate.
202059377	True	True	Cannot validate candidate.
202066537	True	True	Cannot validate candidate.
202071289	True	True	Cannot validate candidate.
202071401	True	True	Cannot validate candidate.
202071645	True	False	Secondary star sufficiently faint.
202083828	False	True	Same depth for $r = 1''$ aperture.
202088212	True	False	Secondary star sufficiently faint.
202126849	False	False	Secondary star sufficiently faint.
202126852	False	False	Secondary star sufficiently faint.
202126887	False	True	Deeper transit with $r = 1''$ aperture.
202126888	False	True	Same depth for $r = 1''$ aperture.
202565282	True	False	Secondary star sufficiently faint.
203929178	True	True	Cannot validate candidate.
204043888	False	False	Secondary star sufficiently faint.
204489514	False	False	Secondary star sufficiently faint.
204890128	False	True	Same depth for $r = 1''$ aperture.
205029914	True	True	Cannot validate candidate.
205064326	False	True	Shallower transit with $r = 1''$; likely FP.
205148699	True	True	Cannot validate candidate.
205686202	True	True	Cannot validate candidate.
205703094	True	True	Cannot validate candidate.
205916793	False	True	Deeper transit with $r = 1''$ aperture.
205999468	False	True	Same depth for $r = 1''$ aperture.
206011496	True	True	Cannot validate candidate.
206061524	True	True	Cannot validate candidate.
206192335	True	True	Cannot validate candidate.
207389002	False	False	Secondary star sufficiently faint.
207475103	True	True	Cannot validate candidate.
207517400	True	True	Cannot validate candidate.
207739861	False	True	Cannot validate candidate.
208445756	False	True	Cannot validate candidate.
209036259	False	True	Cannot validate candidate.
210401157	True	True	Cannot validate candidate.
210414957	True	True	Cannot validate candidate.
210513446	True	True	Cannot validate candidate.
210666756	True	True	Cannot validate candidate.
210958990	True	True	Cannot validate candidate.
211089792	False	True	Same depth for $r = 1''$ aperture.
211147528	True	True	Cannot validate candidate.

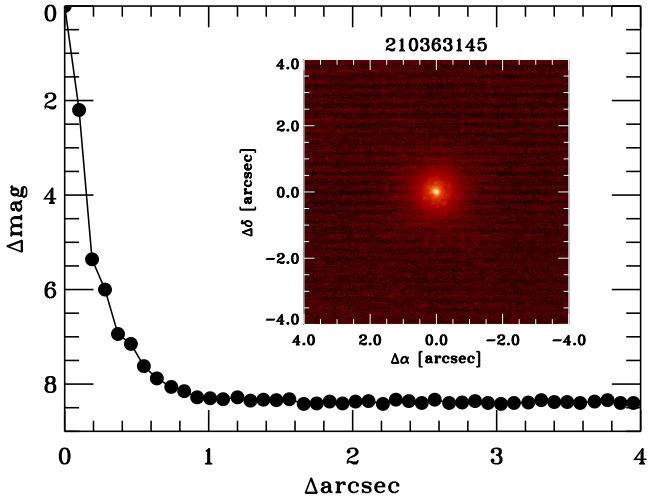

Figure 4. Example constraints on any additional, nearby stars around K2-77 (EPIC 210363145) from Keck/NIRC2 *K*-band adaptive optics imaging. For this target, no companions were detected above the plotted contrast limits. Detected stellar companions around all observed candidates are listed in Table 5.

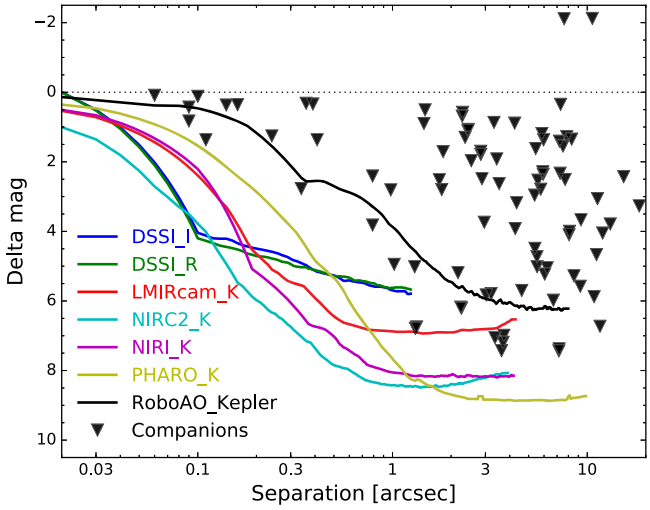

Figure 5. Stellar companions (triangles) detected near our *K2* candidate systems and the median contrast achieved with each listed instrument and filter (solid curves). As described in Section 3.3, these detected magnitude differences set upper limits on the maximum amount of blending possible within the *Kepler* bandpass. Parameters of these nearby stars are listed in Table 5.

irradiation ($S_{\rm inc}$). We use several complementary techniques to infer stellar parameters for our entire sample.

For all stars with Keck/HIRES and/or APF/Levy spectra, we attempt to estimate effective temperatures, surface gravities, metallicities, and rotational velocities using `SpecMatch` (Petigura 2015). `SpecMatch` fits a high-resolution optical spectrum to an interpolated library of model spectra from Coelho et al. (2005), which closely match the spectra of well-characterized stars in this temperature range. Uncertainties on $T_{\rm eff}$, $\log g$, and [Fe/H] from HIRES spectra are 60 K, 0.08–0.10 dex, and 0.04 dex, respectively (Petigura 2015). Experience shows that `SpecMatch` is limited to stars with $T_{\rm eff} \sim 4700$–6500 K and $v \sin i \lesssim 30$ km s^{-1}.

The `SpecMatch` pipeline used to analyze the APF data is identical to the Keck `SpecMatch` pipeline, except we employ the differential-evolution Markov Chain Monte Carlo (DE-MCMC; Ter Braak 2006) fitting engine from ExoPy (Fulton et al. 2013) instead of χ^2 minimization. The APF `SpecMatch` pipeline was empirically calibrated to produce consistent stellar parameters for stars that were observed at both Keck and APF by fitting and subtracting a three-dimensional surface to the residuals of $T_{\rm eff}$, $\log g$, and Fe/H between the calibrated Keck and initial APF parameters. The errors on the stellar parameters are a quadrature sum of the statistical errors from the DE-MCMC fits and the scatter in the APF versus Keck calibration. The scatter in the calibration is generally an order of magnitude

larger than the statistical errors in the S/N regime for the *K2* targets observed on APF.

Petigura (2015) assessed the accuracy of SpecMatch-derived stellar parameters by modeling the spectra of several samples of touchstone stars with well-measured properties. The properties of these stars were determined from asteroseismology (Huber et al. 2012), detailed LTE spectral modeling, and transit light curve modeling (Torres et al. 2012), and detailed LTE spectral modeling (Valenti & Fischer 2005). The uncertainties of SpecMatch parameters are dominated by errors in the Coelho et al. (2005) model spectra (e.g., inaccuracies in the line lists, assumption of LTE, etc.). Given that we observe spectra at S/N $\gtrsim$ 35 per pixel, photon-limited errors are not an appreciable fraction of the overall error budget.

To estimate stellar masses and radii for all stars with SpecMatch parameters, we use the free and open source isochrones Python package (Morton 2015a). This tool accepts as inputs the $T_{\rm eff}$, $\log g$, and [Fe/H] measured by SpecMatch and interpolates over a grid of stellar models from the Dartmouth Stellar Evolution Database (Dotter et al. 2008). isochrones uses the emcee Markov Chain Monte Carlo package (Foreman-Mackey et al. 2012) to estimate uncertainties, sometimes reporting fractional uncertainties as low as 1%. Following Sinukoff et al. (2016), we adopt a lower limit of 5% for the uncertainties on stellar mass and radius to account for the intrinsic uncertainties of the Dartmouth models found by Feiden & Chaboyer (2012).

Eighty-five stars in our sample lack SpecMatch parameters. For most of these, we adopt the stellar parameters of Huber et al. (2016). This latter analysis relies on the Padova set of stellar models (Marigo et al. 2008), which systematically underestimate the stellar radii of low-mass stars. Follow-up spectroscopy to provide refined parameters for these later-type stars is underway (C. Dressing et al. 2016, in preparation; A. Martinez et al. 2016, in preparation). Our sample includes a small number of stars not considered by Huber et al. (2016), such as targets in *K2*'s Campaign 0. For these, we use isochrones in conjunction with broadband photometry collected from the APASS, 2MASS, and *WISE* surveys to infer the stellar parameters.

We then use the free, open source LDTk toolkit (Parviainen & Aigrain 2015) to propagate our measured $T_{\rm eff}$, $\log g$, [Fe/H], and their uncertainties into limb-darkening coefficients and associated uncertainties. These limb-darkening parameters act as priors in our transit light curve analysis (described below in Section 5). We upgraded LDTk to allow the (typically non-Gaussian) posterior distributions generated by the isochrones package to be fed directly into the limb-darkening analysis.[40] Because LDTk often reports implausibly small uncertainties on the limb-darkening parameters, based on our experience with such analyses we increase all these uncertainties by a factor of five in our light curve analyses. Spot checks of a number of systems reveal that imposing priors on the stellar limb-darkening has a negligible impact ($<1\sigma$) on our final results, relative to analyses with much weaker constraints on limb darkening.

All our derived stellar parameters—$T_{\rm eff}$, $\log g$, $R_\star$, $M_\star$—and their uncertainties are listed in Table 7.

[40] GitHub commits 60174cc, 46d140b, and 8927bc6.

5. TRANSIT LIGHT CURVE ANALYSES

After identifying planet candidates and determining the parameters of their host stars, we subject the detrended light curves to a full maximum-likelihood and MCMC analysis. We use a custom Python wrapper of the free, open source BATMAN light curve code (Kreidberg 2015). We upgraded the BATMAN codebase to substantially increase its efficiency when analyzing long-cadence data.[41] The light curves are fit using the standard Nelder-Mead Simplex Algorithm[42] and then run through emcee to determine parameter uncertainties.

Our general approach follows that used in our previous papers (Crossfield et al. 2015; Petigura et al. 2015; Schlieder et al. 2016; Sinukoff et al. 2016). The model parameters in our analysis are the transit time (T_0); the candidate's orbital period and inclination (P and i); the scaled semimajor axis (a/R_*); the fractional candidate size (R_p/R_*); the orbital eccentricity and longitude of periastron (e and ω), the fractional level of dilution (δ) from any other sources in the aperture; a single multiplicative offset for the absolute flux level; and quadratic limb-darkening coefficients (u_1 and u_2). We initialize each fit with the best-fit parameters returned from TERRA. Note that both this analysis and that of TERRA assume a linear ephemeris, so systems with large transit timing variations (TTVs) could be missed or misidentified.

During the analysis, several parameters are constrained or subjected to various priors. Gaussian priors are applied to the limb-darkening parameters (as derived from the LDTk analysis), to P (with a dispersion of $\sigma_P = 0.01$ days, to ensure that the desired candidate signal is the one being analyzed), and to e ($\mu_e = 10^{-4}$ and $\sigma_e = 10^{-3}$, to enforce a circular orbit). We also apply a uniform prior to T_0 (with width $0.06P$), i (from 50° to 90°), R_p/R_* (from -1 to 1), and ω (from 0 to 2π); both P and a/R_* are furthermore constrained to be positive. Allowing R_P/R_* to take on negative values avoids the Malmquist bias that would otherwise result from treating it as a positive-definite quantity. For those systems with no identified stellar companions, our HRI and/or spectroscopy constrain the dilution level; otherwise, we adopt a log-uniform prior on the interval (10^{-6}, 1).

6. FALSE POSITIVE ASSESSMENT

During the prime *Kepler* mission, both the sheer number of planet candidates and their intrinsic faintness made direct confirmation by RVs impractical for most systems. Nonetheless many planets can be statistically validated by assessing the relative probabilities of planetary and false positive scenarios; a growing number of groups have presented frameworks for quantitatively assessing the likelihoods of planetary and false positive scenarios (Torres et al. 2011; Morton 2012; Díaz et al. 2014; Santerne et al. 2015). These false positive scenarios come in several classes: (1) undiluted eclipsing binaries, (2) background (and foreground) eclipsing binaries where the eclipses are diluted by a third star, and (3) eclipsing binaries in gravitationally bound triple systems.

To estimate the likelihood that each of our planet candidates is a true planetary system or a false positive configuration, we use the free and open source vespa software (Morton 2015). vespa compares the likelihood of each scenario against the planetary interpretation and accepts additional constraints from

[41] GitHub commit 9ae9c83.

[42] As implemented in scipy.optimize.fmin.

Table 7
Stellar Parameters

EPIC	Kp (mag)	R_* ($R_\odot$)	M_* ($M_\odot$)	T_{eff} (K)	log g (dex)	Source
201155177	14.632	0.643(39)	0.702(46)	4613(71)	4.659(50)	Huber et al. (2016)
201176672	13.980	0.508(98)	0.559(87)	4542(130)	4.747(97)	Huber et al. (2016)
201205469	14.887	0.570(30)	0.600(30)	3939(87)	4.698(23)	Huber et al. (2016)
201208431	14.409	0.435(60)	0.487(72)	4044(81)	4.849(60)	Huber et al. (2016)
201247497	16.770	0.436(27)	0.492(29)	3918(46)	4.846(50)	Huber et al. (2016)
201295312	12.126	1.58(15)	1.150(60)	5912(51)	4.101(63)	SpecMatch
201324549	12.146	1.45(25)	1.18(12)	6283(113)	4.17(12)	Huber et al. (2016)
201338508	14.364	0.462(38)	0.520(44)	4021(62)	4.823(50)	Huber et al. (2016)
201345483	15.319	0.445(66)	0.503(78)	4103(90)	4.824(70)	Huber et al. (2016)
201367065	11.574	0.371(50)	0.414(58)	3841(82)	4.906(60)	Huber et al. (2016)
201384232	12.510	1.010(80)	0.930(30)	5767(58)	4.398(74)	SpecMatch

(This table is available in machine-readable form.)

HRI and spectroscopy. Throughout this analysis, we apply Version 0.4.7 of `vespa` (using the MultiNest backend) to each individual planetary candidate. Other types of false positive scenarios exist that are not explicitly treated by `vespa`, such as eclipsing binaries on eccentric, inclined orbits showing only transit or occultation (but not both), or extremely inconvenient arrangements of starspots. The community's experience of following up transiting planet candidates indicates that such scenarios are much less common than those considered by `vespa`; nonetheless quantifying the likelihood of such scenarios for each candidate would be an interesting avenue for future research.

6.1. Calculating FPPs

To calculate the FPP for each system, we use the following inputs: stellar photometry from APASS, 2MASS, and *WISE*; the stellar parameters described in Section 4; the detrended light curve (after masking out any transits from other candidates in that system); the exclusion constraints from adaptive optics imaging data in terms of contrast versus separation (where available) and from our high-resolution spectroscopy (maximum allowed contrast and velocity offset); and an upper limit on the depth of any secondary eclipse. We derive the last of these by constructing a rectangular signal with depth unity and duration equal to the best-fit transit duration, scanning the template signal across the out-of-transit light curve, and reporting the 99.7th percentile as the eclipse depth's upper limit.

We report the final FPPs of all our systems in Table 8. For the purposes of the discussion that follows, we deem any candidate signal with FPP < 0.01 as a validated extrasolar planet and signals with FPP > 0.99 as false positives. For all unvalidated candidates, Table 9 summarizes `vespa`'s estimate of the relative (unnormalized) likelihood of each potential false positive scenario.

The `vespa` algorithm implicitly assumes that each planet candidate lacks any other companion candidates in the same system. Studies of *Kepler*'s multiple-candidate systems show that almost all are planets (Lissauer et al. 2012). This "multiplicity boost" has subsequently been used to validate hundreds of multi-planet systems (Rowe et al. 2014). Because `vespa` treats only single-planet systems, we simply treat these multi-candidate systems as independent, isolated candidates in the FPP analysis. Sinukoff et al. (2016) show that *K2*'s multiplicity boost is $\geqslant$20 even in crowded fields, comparable to the boost factor derived for the original *Kepler* mission.

Even without the multiplicity boost, our approach validates the majority of our multi-candidate systems. Both EPIC 201445392 (K2-8) and EPIC 206101302 host two-planet candidates. In each system we validate one candidate and find FPP $= 4\%$–7% for the other. The *K2* multiplicity boost factor of $\geqslant$20 therefore results in all candidates in both systems being firmly labeled as validated planets.

A more complicated case is EPIC 205703094, which hosts three planet candidates. Our `vespa` analysis finds that one candidate is a false positive and that the others both have FPP $\approx 50\%$ (see Tables 8 and 9). Our light curve analysis finds that all three candidates are well-fit by grazing transits ($b \sim 1$), leaving R_P/R_* only weakly constrained. Furthermore, our HRI reveals that the system is a close visual binary with separation $0\farcs14$ (see Tables 6 and 5). Therefore we can neither validate nor rule out the three candidates in this system.

6.2. Targets with Nearby Stellar Companions

Planet candidates orbiting stars in physical or visual multiple systems are much more difficult to validate due to blending in the photometric aperture (see, e.g., Ciardi et al. 2015). Table 5 shows that our *K2* photometric apertures are quite large (up to $20''$ in extreme cases) and that HRI follow-up reveals stellar companions within these apertures for many systems. Therefore we must treat these systems with greater care.

To demonstrate the difficulty, consider two stars with flux ratio $F_2/F_1 < 1$ and angular separation ρ. Assume both lie in a photometric aperture with radius $r > \rho$, with which a transit is observed with apparent depth δ'. If the transit occurs around the primary star, then the true transit depth is $\delta_1 \approx \delta'/(1 - F_2/F_1)$; this is at most twice the observed depth, indicating a planetary radius up to $\sqrt{2}$ larger than otherwise determined. If instead the transiting object orbits the secondary, then the true transit depth is $\delta_2 \approx \delta' F_1/F_2$ and the transiting object may be many times larger than expected. Table 6 lists all candidates known to host secondary stars and their relationships between F_2/F_1 & δ' and ρ & r.

Any planet candidate in a multi-star system and with $F_2/F_1 < \delta'$ cannot transit the secondary (which is too faint to be the source of the observed transit signal). We find several

Table 8
Planet Candidate Parameters

Other Name	EPIC	P (d)	T_0 (BJD_{TDB} –2454833)	T_{14} (hr)	R_P/R_* (%)	a (au)	R_P ($R_\oplus$)	S_{inc} ($S_\oplus$)	FPP	Disposition
K2-42b	201155177.01	6.68796(93)	1981.6763(52)	3.04(20)	3.04(28)	0.0617(13)	2.15(24)	44.1(6.3)	5.2e−07	Planet
	201176672.01	79.9999(98)	2044.8046(15)	11.75(17)	18.0(1.1)	0.299(16)	10.2(2.1)	1.10(46)	0.094	Candidate (see Tables 6 and 1)
K2-43b	201205469.01	3.47114(21)	1976.8845(33)	1.97(11)	6.60(36)	0.03784(63)	4.13(31)	49.0(6.9)	9.7e−10	Planet
K2-4b	201208431.01	10.0044(11)	1982.5170(45)	2.87(17)	3.49(41)	0.0715(35)	1.69(30)	8.9(2.7)	0.00028	Planet
	201247497.01	2.75391(15)	1977.9031(23)	1.03(14)	7.9(1.3)	0.03035(59)	3.78(68)	43.7(6.1)	0.41	Candidate
K2-44b	201295312.01	5.65688(59)	1978.7176(44)	4.36(13)	1.56(12)	0.0651(11)	2.72(32)	646(126)	6.7e−07	Planet
	201324549.01	2.519334(35)	1976.99353(69)	1.545(15)	2.41(30)	0.0383(13)	3.91(85)	2002(727)	1	False Positive (see Tables 6 and 3)
K2-5c	201338508.01	10.9324(14)	1981.6012(55)	2.84(23)	3.24(29)	0.0775(22)	1.64(20)	8.3(1.6)	2.8e−05	Planet
K2-5b	201338508.02	5.73597(68)	1975.8602(53)	2.35(18)	2.97(22)	0.0504(14)	1.50(17)	19.7(3.7)	5.4e−06	Planet
K2-45b	201345483.01	1.7292684(69)	1976.52604(18)	1.689(14)	13.76(19)	0.0224(12)	6.71(00)	100(32)	6.8e−06	Planet
K2-3b	201367065.01	10.05443(26)	1980.4178(12)	2.520(59)	3.51(15)	0.0679(32)	1.44(20)	5.8(1.7)	1.9e−08	Planet
K2-3c	201367065.02	24.6435(12)	1979.2811(24)	3.38(12)	2.88(16)	0.1235(58)	1.18(17)	1.77(53)	2.1e−08	Planet
K2-3d	201367065.03	44.5609(52)	1993.2285(34)	4.04(19)	2.35(15)	0.1833(86)	0.96(14)	0.80(24)	1.2e−07	Planet

Note. Table 8 is published in its entirety in the machine-readable format. A portion is shown here for guidance regarding its form and content.

(This table is available in its entirety in machine-readable form.)

Table 9
Unvalidated Candidate False Positive Likelihoods

Target	L_heb[a]	L_heb_P × 2[a]	L_eb[b]	L_eb_P × 2[b]	L_beb[c]	L_beb_P × 2[c]	L_pl[d]	FPP
201176672.01	3.2e−36	0.0097	7.3e−19	0.046	0.002	0.0019	0.035	0.094
201247497.01	7.2e−16	7.4e−05	2.6	20	0	2.9	12	0.41
201445392.01	0.00027	0.028	0.042	0.83	0	0.081	1.5	0.042
201465501.01	0.00047	0.19	0.0036	0.46	0	0.015	0.042	0.45
201512465.01	0.0021	0.09	0.013	0.82	1.3	5.6	8.3	0.23
201546283.01	6e−15	1e−07	8.1e−10	5.4e−16	0.0019	0.00045	14	4.4e−07
201565013.01	3.6e−07	0.073	16	1.2	1.1	0.44	8	0.76
201617985.01	0.0048	0.77	0.0046	1.5	0.09	0	0.025	0.96
201626686.01	5.5e−20	1.1e−10	0.3	0.012	4.6e−05	5.6e−07	1.6	0.16
201629650.01	5.9e−69	2.3e−21	1.2e−07	1.1e−08	5.2e−11	1.2e−39	0.002	3.6e−05
201637175.01	4	1.3	0.23	15	0.17	2.2	19	0.15
201702477.01	1.6e−12	2.9e−06	0.13	0.0048	0.19	0.021	0.79	0.41
201717274.01	7e−12	1.6e−05	3.9e−08	0.00016	0.25	0.71	8.9	0.013
201828749.01	1.4e−14	1.1e−13	5.4e−09	5.3e−28	0	0	0.059	3.3e−08
201862715.01	2.2e−23	4e−09	6.8e−18	4.5e−13	0.014	2.3e−07	5.8	2.4e−07
201920032.01	7.9e−34	2.4e−10	0.078	0.056	0.0014	0	0.99	0.054
202071289.01	0.076	0.96	4.5	3.5	0.00015	1.9e−08	11	0.97
202071401.01	0.0062	0.16	0.0086	0.27	0	7.1e−05	2.5	0.002
202126852.01	0.059	0.0024	4.2	0.036	0	0.015	2.8	0.65
202675839.01	0.045	0.19	0.18	0.24	1e−14	0	0.46	0.19
205029914.01	2e−34	5.4e−10	1e−34	4.7e−16	0	3.3e−12	0.0054	1.4e−10
205148699.01	5.4e−58	4.7e−34	6.5e−31	1.2e−48	0	0	0.81	0
205570849.01	0.041	0.38	0.78	0.48	0	4.7e−25	1.2	0.32
205686202.01	1.8e−36	3.2e−16	2.7e−40	7e−11	2e−08	0	2.5	1.3e−11
205703094.02	0.0027	0.049	0.0011	0.034	0.0073	0.0097	0.13	0.66
205999468.01	0.056	0.85	0.96	1.2	0.43	1.1	2.8	0.1
206011496.01	4.1e−26	1.7e−06	4.4e−15	1.4e−05	0	0	12	1.6e−08
206024342.01	3e−07	6.6e−06	0.021	0.027	0	0	0.84	0.025
206028176.01	0.0024	0.072	0.015	0.1	0	0	0.0065	0.64
206036749.01	1.3	1.3	1.6	0.59	0	0	2.1	0.097
206061524.01	4.7e−22	1e−08	1.1e−16	3.7e−18	0.0023	5e−08	36	4.6e−08
206101302.01	0.00036	0.0023	0.051	0.085	0.072	0	0.61	0.069
206114294.01	0.0083	0.16	0.46	2	0	0	19	0.028
206154641.01	0.00065	0.016	2.1	0.059	0	0	15	0.074
206192335.01	1.4e−08	0.0042	2.1e−05	0.022	0	0	11	6e−05
206247743.01	8.7e−78	2.6e−22	8.5e−26	3.2e−06	0	0	2.3e−06	0.025
206403979.01	1.2e−08	8.5e−07	0.13	0.06	0.015	0.012	0.26	0.72
206543223.01	0.045	0.25	1.2	0.0046	0.0016	0.021	2.2	0.67
207739861.01	3.5e−203	1.4e−80	1.4e−66	2.6e−21	0	0	2.4e−05	1.1e−16
208833261.01	0	8.9e−196	1.1e−05	0.00091	0.23	0.25	2.5	0.011
209036259.01	0	4e−40	3.9e−19	0.075	0	0	0.00059	0.96
210389383.01	4.3e−77	3.8e−64	5.2e−07	6.2e−39	6.9e−05	3.4e−09	2.4	4.1e−05
210609658.01	2.5e−146	2.3e−20	3.3e−13	0.0098	3.7e−18	6.6e−12	0.0077	0.015
210625740.01	2.3	0.86	0.18	5	0.036	1.5	31	0.13
210659688.01	0.017	0.012	0.016	0.073	0.016	0.023	0.17	0.25
210666756.01	5.3	0	0.42	2.8	0.055	0.37	2.4	0.013
210754505.01	1e−07	0.015	15	0.8	0	1.6	1.5	0.24
210903662.01	4.1	5.2	12	7.9	0.61	0	7	0.59
210958990.01	3.8	0.0015	0.01	9.1e−16	0.41	1.1e−09	0.032	0.98
211147528.01	0.018	0.00047	0.45	0.003	0.47	0.053	1.8	0.26
211916756.01	1.3e−33	2.7e−09	1e−28	2.3e−09	0.9	0.43	0.003	0.88

Notes.
[a] Likelihood that the system is a hierarchical eclipsing binary, with orbital period either as measured or twice that measured.
[b] Likelihood that the system is an eclipsing binary, with orbital period either as measured or twice that measured.
[c] Likelihood that the system is a blended eclipsing binary, with orbital period either as measured or twice that measured.
[d] Likelihood that the system is a transiting planet.

(This table is available in machine-readable form.)

such systems, though only two (EPIC 202126852 and 211147528) have FPP < 0.95. Nonetheless, for all these systems we account for the dilution of the secondary star(s) as described below.

For candidates with $\delta' < F_2/F_1$ and $\rho < r$, the transit could occur around either star. We compare our nominal time-series photometry to that computed with $r = 1$ pixel for all such candidates. For targets with more widely separated nearby

Table 10
High-resolution Imaging

EPIC	Filter	t_{int} (s)	Instrument
201155177	K	330	NIRI
201176672	K	270	NIRC2
201205469	K	810	NIRC2
201208431	K	171	NIRC2
201247497	K	540	NIRC2
201295312	K	212.4	PHARO
201295312	K	225	NIRC2
201324549	K	276.1	PHARO
201324549	K	300	NIRI
201338508	K	1080	NIRC2

(This table is available in its entirety in machine-readable form.)

stars, if the one-pixel-photometry reveals a shallower transit, then the transit probably occurs around the secondary star. However, if $\rho < 1$ pix then we cannot reliably identify the source of the transits. We find 28 candidates of these types that we cannot validate at present, and note the disposition of all such systems in Table 6.

For all remaining systems, the detected transits must occur around the primary star but will be diluted by light from the secondary. We estimate the total brightness of these systems' secondary star(s) as follows. For stars detected by optical imaging (Robo-AO and DSSI), we use the measured contrast ratio with an uncertainty of 0.05 mag. For stars detected by infrared imaging, we use the relations of Howell et al. (2012) to translate the observed infrared color into the *Kepler* bandpass. Since these relations are approximate and depend strongly on SpT, we conservatively apply an uncertainty of 0.5 mag to these values. Section 6.2 describes how we use these data to constrain the dilution parameter's posterior distribution, thereby reducing the systematic biases induced by unrecognized sources of dilution (e.g., Ciardi et al. 2015).

7. RESULTS AND DISCUSSION

We find 104 validated planets (i.e., FPP < 0.01) in our set of 197 planet candidates. Significantly, we show that *K2*'s surveys increase by 30% the number of small planets orbiting moderately bright stars compared to previously known planets. In Section 7.1 we present a general overview of our survey results. Then, in Section 7.2 we discuss individual systems, both new targets and previously identified planets and candidates.

7.1. Overview of Results

Our validated planetary systems span a range of properties, with median values of $R_P = 2.3\,R_\oplus$, $P = 8.6$ days, $T_{\rm eff} = 5300$ K, and $Kp = 12.7$ mag. Figure 7 shows the distribution of planet radius, orbital period, and final disposition for our entire candidate sample. The candidates range from 0.7 to 44 days, and from $<1R_\oplus$ to larger than any known planets.

Figure 8 shows that the majority of candidates have $R_P < 3R_\oplus$, and these smallest candidates exhibit the highest validation rates. In contrast, we validate less than half of candidates with $R_P > 3R_\oplus$ and less than half of candidates with $P < 2$ days (Figure 1). We find a substantially higher validation rate for target stars cooler than ~5500 K versus hotter stars (65% versus 37%; see Figure 9). Figure 10 shows that we validate no systems with $Kp > 16$ mag, but otherwise reveals no obvious trends with stellar brightness.

Our analyses leave 63 planet candidates with no obvious disposition (i.e., $0.01 < \mathrm{FPP} < 0.99$). These candidates are typically large ($R_P > 3R_\oplus$), and their FPPs are listed in Table 8. Furthermore, in Table 9 we list the individual likelihoods of each false positive scenario considered by `vespa`.

We calculate the FPR of our entire planet candidate sample by taking our 197 candidates, excluding the 28 candidates with nearby stars discovered by HRI that we cannot validate (see Section 6.2), and integrating over the probability that each candidate is a planet. In this way we estimate that our entire sample contains roughly 145 total planets (though we validate just 104). This ratio corresponds to a false positive rate of 15%–30%, with higher FPPs for candidates showing larger sizes and/or shorter orbital periods (see Figures 1 and 8).

We also split our sample into several bins in radius and period to estimate the FPR for each subset, listed in Table 2. Our FPR is dominated by larger candidates, just as Figure 8 suggests. Sub-Jovian candidates (with $R_P \leqslant 8R_\oplus$) have a cumulative FPR of ~10%, whereas over half of the larger candidates are likely false positives. The FPR for larger candidates is consistent with that measured for the original *Kepler* candidate sample (Santerne et al. 2016b). Candidates with $P < 3$ days have a FPR roughly twice as high as that for longer-period systems.

Since we have excluded the 28 candidates described above, these FPRs are only approximate and we defer a more detailed analysis of our survey completeness and accuracy to a future publication. Nonetheless, further follow-up observations for systems lacking high-resolution spectroscopy, HRI, and/or RV measurements may expect to identify, validate, and confirm a considerable number of additional planetary systems.

Figure 11 shows planet radius versus the irradiation levels incident upon each of our validated planets relative to that received by the Earth ($S_\oplus$), color-coded by $T_{\rm eff}$. These planets receive a wide range of irradiation, from roughly that of Earth to over $10^4\times$ greater. As expected, our coolest validated planets orbit cooler stars (K and M dwarfs). However, we caution that the stellar parameters for these systems come from broadband colors and/or Huber et al. (2016), so uncertainties are large and biases may remain. Follow-up spectroscopy is underway to more tightly constrain the stellar and planetary properties of these systems (C. Dressing et al. 2016, in preparation; A. Martinez et al. 2016, in preparation).

Finally, Figure 12 shows that *K2* planet survey efforts have substantially increased the number of smaller planets known to orbit moderately bright stars. Although our sensitivity appears to drop off below $\sim 1.3R_\oplus$ (as shown in Figure 8) and we find no planets around stars brighter than $J < 8.9$ mag, we validate a substantial number of intermediate-size planets around moderately bright stars. In particular, the right panel of Figure 12 shows that the first five fields of *K2* have already increased the number of small planets orbiting fairly bright stars by roughly 30% compared to those tabulated at the NASA Exoplanet Archive. Considering the sizes of these planets and the brightness of their host stars, many of these systems are amenable to follow-up characterization via Doppler spectroscopy and/or *JWST* transit observations.

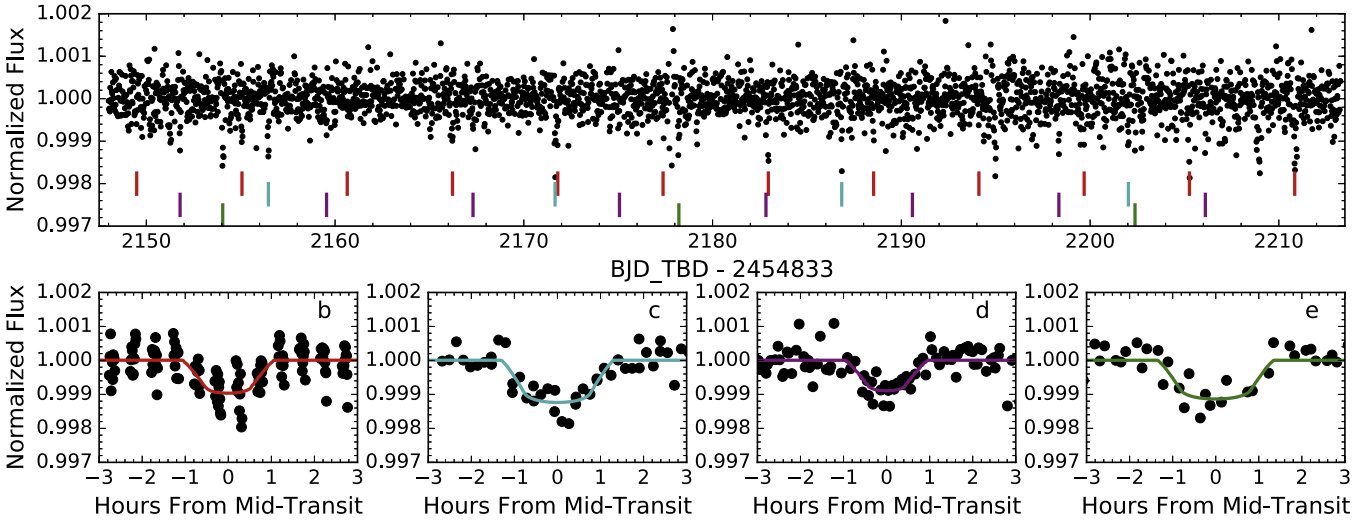

Figure 6. Photometry of K2-72 (EPIC 206209135), which hosts four transiting planets. Top: full time-series, with colored tick marks indicating each individual transit time. Bottom: phase-folded photometry with the color-coded, best-fit transit model overplotted for each planet. Our analysis indicates a stellar radius of $0.40^{+0.12}_{-0.07}$ $R_{\odot}$, planetary radii of 1.2–1.5$R_{\oplus}$, and (from left to right) orbital periods of 5.58, 7.76, 15.19, and 24.16 days.

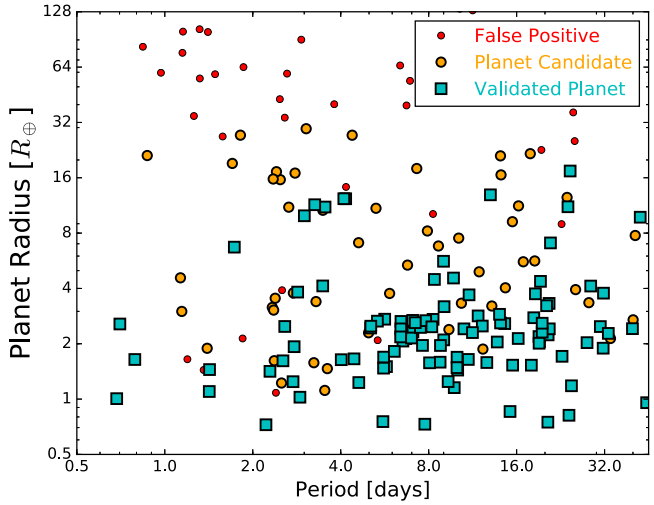

Figure 7. Orbital periods and radii of our 104 validated planets, 30 false positive systems, and 63 remaining planet candidates. Uncertainties on planet radius (listed in Table 8) are typically ∼13%.

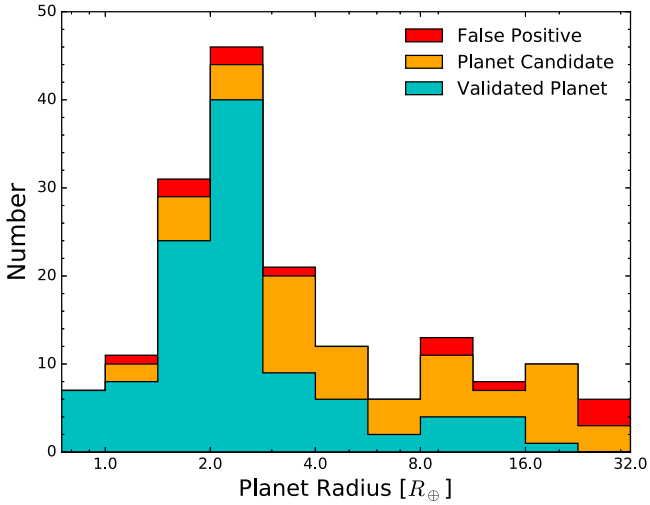

Figure 8. Distribution of planet candidate radii for our validated planets, false positive systems, and remaining planet candidates. We validate most of the candidates smaller than 3 $R_{\oplus}$, consistent with the low false positive rate we find for small planets.

7.2. Notes on Individual Systems

Of the 104 planets validated by our analysis, 64 are newly validated. These include several new multi-planet systems, systems as bright as $V = 10.8$ mag, and several small, roughly Earth-sized planets receiving roughly Earth-like levels of irradiation. Below we describe some of the most interesting new systems in Section 7.2.1, our analysis of previously confirmed or validated planets in Section 7.2.2, and our results for known but unvalidated candidates in Section 7.2.3.

7.2.1. New Validated Planets

K2-72 (EPIC 206209135) is a dwarf star hosting a planet candidate on a 5.57 day orbit (Vanderburg et al. 2016); we find three additional candidates and validate all four planets in this system. We see the transits in both our photometry (shown in Figure 6) and that of Vanderburg & Johnson (2014), and our light curve fits give consistent values of $\rho_{*,\mathrm{circ}}$ for all planets—both points give us confidence that these are true planetary systems. Huber et al. (2016) reports a stellar radius of 0.23 $R_{\odot}$ but notes that this is likely an underestimate. The weighted mean of our four stellar density measurements is 9.0 ± 3.6 g cm^{-3}; using the mass–radius relation of Maldonado et al. (2015) implies a stellar radius of $0.40^{+0.12}_{-0.07}$ $R_{\odot}$ and planetary radii of 1.2–1.5 $R_{\oplus}$ for all planets. Analysis of the stellar spectrum is also consistent with this size (C. Dressing et al. 2016, in preparation; A. Martinez et al. 2016, in preparation). These four small planets have orbital periods of 5.58, 7.76, 15.19, and 24.16 days. The irradiation levels for several planets are also quite consistent with Earth's insolation. Several of these planet pairs orbit near mean-motion resonances: planets c and d orbit near the first-order 2:1 MMR, and b and c orbit near the second-order 7:5 MMR. Although the star K2-72 is relatively faint—$Kp = 14.4$ mag, $K = 11.0$ mag — follow-up Doppler or transit spectroscopy observations to measure the planets' masses or atmospheric compositions will be challenging; the system's near-integer period ratios suggest

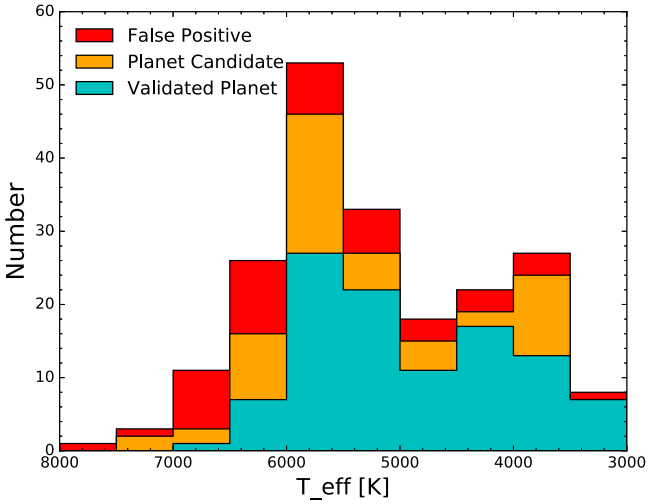

Figure 9. Distribution of stellar effective temperatures for systems with validated planets, false positive, and remaining planet candidates. There is a hint of a higher validation rate around stars cooler than ∼5500 K.

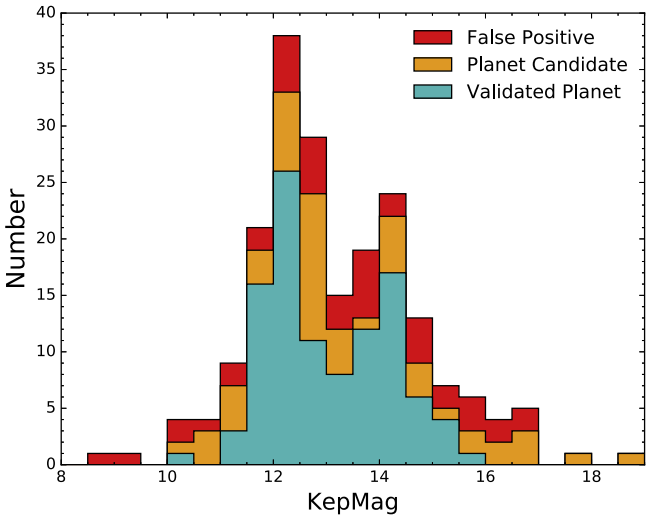

Figure 10. Distribution of *Kp* for systems with validated planets, false positives, and remaining planet candidates. Our brightest validated system, K2-65 (EPIC 206144956), contains a 1.6 $R_\oplus$ planet orbiting a $V = 10.8$ mag star.

that measurements of TTVs may help reveal the masses and bulk densities of all these planets.

We also identify and validate four new two-planet systems in Campaign 4: K2-80, K2-83, K2-84, and K2-90 (EPIC 210403955, 210508766, 210577548, and 210968143, respectively). Our light curve analyses of the planets in each system yield values of $\rho_{*,\mathrm{circ}}$ that are consistent at $<1\sigma$, consistent with the hypothesis that both planets in each pair orbit the same star. Future transit follow-up of these systems will be challenging but feasible, with the most easily observed transits having depths of ∼1 mmag. None of the systems appear to have planets near low-order mean-motion resonance, but additional (non-transiting) planets in these systems could lie near resonance and induce detectable TTVs.

Our brightest validated system, K2-65 (EPIC 206144956), contains a 1.6 $R_\oplus$ planet orbiting a star with $V = 10.8$ mag, $J = 9.0$ mag located in Campaign 3. Despite its 13-day orbital period and low predicted RV semi-amplitude (likely $\lesssim 1\ \mathrm{m\,s^{-1}}$), the bright star, relatively small planet size,

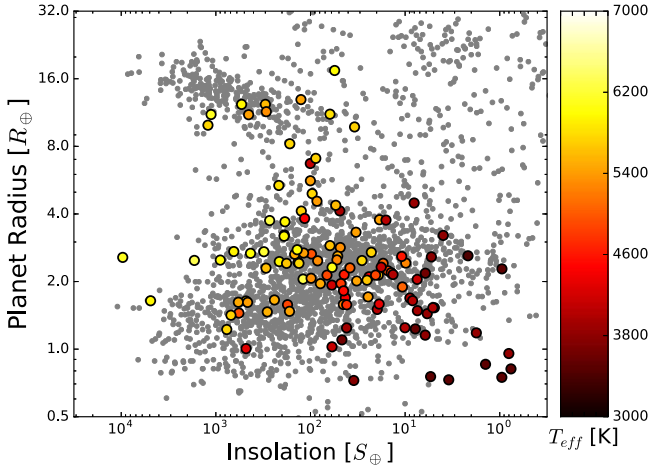

Figure 11. Planetary radii, incident insolation, and stellar effective temperature for our 104 validated planets (colored points) and all planets at the NASA Exoplanet Archive (gray points). As expected, most of our smaller, cooler planets are found around cooler, later-type stars ($T_{\mathrm{eff}} \lesssim 4000$ K). Uncertainties, omitted for clarity, are listed in Table 8. Statistical uncertainties on planet radius and insolation (listed in Table 8) are typically ∼13% and ∼26%, respectively, but the coolest host stars are likely larger, hotter, and more luminous than they appear (Huber et al. 2016).

and low planet insolation (just 45× that of Earth's) may make this system an attractive target for future RV efforts.

Also of interest for RV follow-up is K2-89 (EPIC 210838726), which hosts a highly irradiated, roughly Earth-sized planet on a one-day orbit around an M dwarf. The planet should have a RV semi-amplitude of roughly $1\ \mathrm{m\,s^{-1}}$, and although the star is not especially bright ($Kp = 13.3$ mag, $K = 10.1$ mag) detection of the planet's RV signal may lie within reach of existing and planned high-precision Doppler spectrographs.

7.2.2. *Previously Confirmed Planets*

K2-3bcd and K2-26b (EPIC 201367065 and 202083828, respectively) were previously validated as sub-Neptune-sized planets orbiting M dwarfs (Crossfield et al. 2015; Schlieder et al. 2016), and K2-3b was confirmed by Doppler spectroscopy (Almenara et al. 2015). Transits of all four planets were also recently observed by *Spitzer* (Beichman et al. 2016). We independently validate all these planets. Note, however, that the stellar parameters we estimate here for these systems systematically underestimate the more accurate, spectroscopically derived parameters presented in those papers.

K2-10b and K2-27b (EPIC 201577035b and 201546283b, respectively) were previously validated as planets (Montet et al. 2015; Van Eylen et al. 2016a). We find FPP < 0.01 for both, thus independently validating these two planetary systems. A new stellar companion with $\rho = 3''$ and $\Delta i = 5.8$ mag slightly dilutes the latter's transit but does not significantly affect its reported parameters.

We report a new stellar companion with $\rho = 3\farcs2$ and $\Delta K = 5.8$ mag near K2-13b (EPIC 201629650; Montet et al. 2015). This new, faint star is bright enough that it could be the source of the observed transits; we therefore suggest that this previously validated system should be deemed a planet candidate.

WASP-47 (EPIC 206103150) hosts a hot Jupiter (planet b; Hellier et al. 2012), a giant planet on a 1.5 year orbit (c; Neveu-

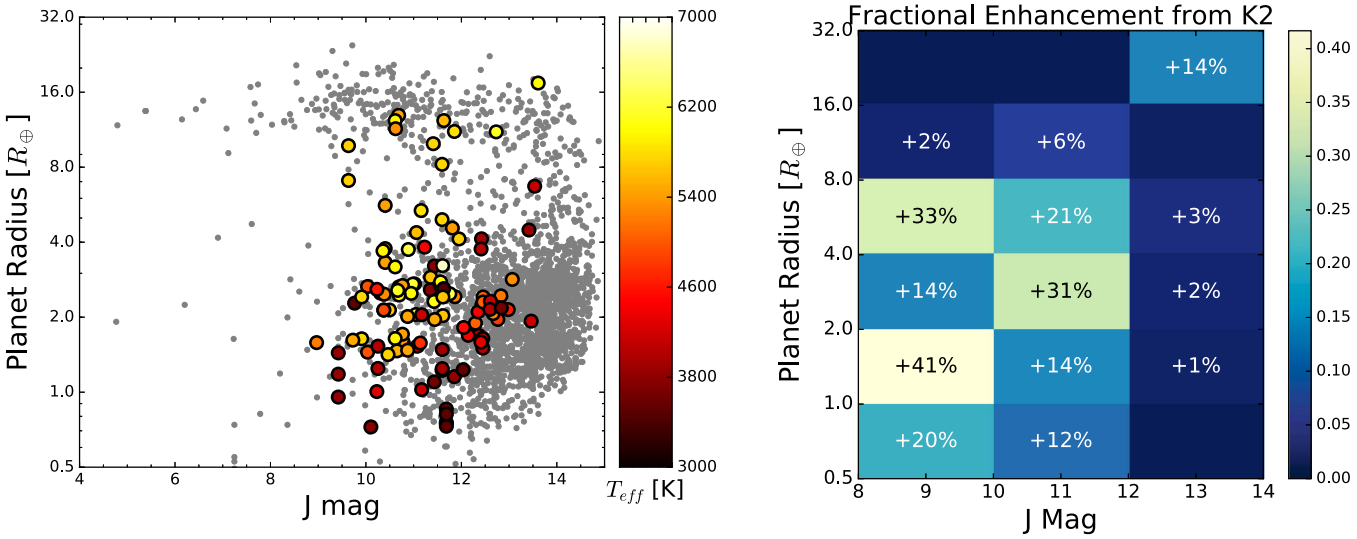

Figure 12. Left: planetary radius, stellar magnitude, and $T_{\rm eff}$ for all validated planets (colored points) and all planets at the NASA Exoplanet Archive (gray points). Right: fractional enhancement by *K2* to the population of known planets. In its first five fields, *K2* has already substantially boosted the numbers of small, bright planets.

VanMalle et al. 2016), and two additional, short-period transiting planets (d and e; Becker et al. 2015). Our analysis of the three transiting planets yields FPP < 0.01 for each, so we independently validate this planetary system.

HAT-P-56b (EPIC 202126852b) is a hot Jupiter confirmed by measuring the planet's mass with Doppler spectroscopy (Huang et al. 2015). Our analysis indicates that the planetary hypothesis is the most probable explanation for the signal detected, with the next-most-likely scenario being an eclipsing binary (FPP = 65%; see Table 9). However, the RV measurements of Huang et al. (2015) rule out the eclipsing binary scenario favored by `vespa` and thus confirm the planetary nature of this system.

K2-19b and c (EPIC 201505350bc) were identified as a pair of planets with an orbital period commensurability near 3:2 (7.9 and 11.9 days; Armstrong et al. 2015; Narita et al. 2015; Barros et al. 2015). A third candidate with a period of 2.5 days was subsequently identified and validated (Sinukoff et al. 2016), which is not near any low-integer period ratios with the previously identified planets. Our analysis independently validates all three of these planets.

K2-21b and c (EPIC-206011691bc) are two planets with radii of 1.5–2 $R_\oplus$, orbiting near a 5:3 orbital period commensurability (Petigura et al. 2015), and K2-24 b and c (EPIC 203771098bc) are two low-density sub-Saturns orbiting near a 2:1 orbital period commensurability and with masses measured by Doppler spectroscopy (Petigura et al. 2016). Our analysis yields FPP < 0.01 for all four of these planets, thereby confirming their planetary status.

K2-22b (EPIC 201637175b) is a short-period rocky planet caught in the act of disintegrating in a 9 hr period around its host star (Sanchis-Ojeda et al. 2015). Our analysis successfully identifies this as a planet candidate and `vespa` indicates that the planetary hypothesis is the most probable explanation for the signal detected (FPP = 15%; see Table 9). However, because `vespa` cannot account for this system's highly variable transit depths (from 1% to as shallow as $<10^{-3}$) the measured FPP is not reliable. We do not claim to de-validate K2-22b.

K2-25b (EPIC 210490365) is a Neptune-sized planet transiting an M4.5 dwarf in the Hyades (Mann et al. 2016; David et al. 2016b). In our transit search, `TERRA` locked on to this star's 1.8 days rotation period, so we did not identify the planet candidate.

K2-31b (EPIC 204129699b) is a hot Jupiter validated by RV spectroscopy (Grziwa et al. 2015; Dai et al. 2016). Because of the grazing transit the planet radius is only poorly determined. The best-fit planet radius listed in Table 8 is implausibly large given the measured mass; this large radius likely led the `vespa` analysis to incorrectly assign this confirmed planet an FPP of 84%.

K2-28b (EPIC 206318379b) was validated by Hirano et al. (2016) as a sub-Neptune-sized planet transiting an M dwarf. We did not identify the system in our transit search; a subsequent investigation shows that our photometry and transit search code did not properly execute for this system, and was never restarted.

K2-29b and K2-30b (EPIC 211089792 and 210957318) are hot Jupiters whose masses were recently measured via Doppler spectroscopy (Johnson et al. 2016; Lillo-Box et al. 2016; Santerne et al. 2016a). We find FPP < 0.01 for both, and thus independently validate these systems.

The Sun-like star BD+20 594 (EPIC 210848071) is reported to host a planet with a radius of 2.3$R_\oplus$ on a 42-day orbit (Espinoza et al. 2016). Since *K2* observed only two transits of this planet, our transit search did not identify this system (see Section 2.3).

The first large sets of planet candidates and validated planets from *K2* were produced by Foreman-Mackey et al. (2015) and Montet et al. (2015). The former identified 36 planet candidates, of which the latter validated 21. We successfully independently validate all but two of these planets, and find that for both outliers the disagreements are marginal. For K2-8b (EPIC 201445392b) we measure FPP = 4.2%, but as discussed in Section 6 the multiplicity boost suppresses this candidate's FPP and results in a validated planet. However, we measure FPP = 45% for K2-9b (EPIC 201465501), almost 10 times greater than originally reported. We attribute this difference to the stellar parameters reported for this star from our

homogeneous `isochrones` stellar analysis: it reports K2-9 to be an early M dwarf, but a more reliable spectroscopic analysis reveals the star to be a smaller and cooler mid-M dwarf (Huber et al. 2016; Schlieder et al. 2016). The planet K2-9b is successfully validated when we use the spectroscopic parameters in our FPP analysis (Schlieder et al. 2016). The discrepancy highlights the importance of accurate and spectroscopically derived stellar parameters (especially for M dwarfs) when assessing planetary candidates.

Recently, our team validated several new multi-planet systems found by *K2*: K2-35, K2-36, K2-37, and K2-38 (EPIC 201549860, 201713348, 203826436, and 204221263; Sinukoff et al. 2016). Our analysis here uses much of the same machinery as in that work, so it should be of little surprise that we again validate all the planets in these systems.

Most recently, the giant planet K2-39b was confirmed by RV spectroscopy (Van Eylen et al. 2016b). Our analysis finds FPP = 0.025%, independently demonstrating (with high likelihood) that the candidate is a planet.

7.2.3. Previously Identified Candidates

Several planet candidates showing just a single transit each were discovered in *K2* Campaigns 1–3 (Osborn et al. 2016). Since our transit search focuses on shorter-period planets (see Section 2.3), we did not identify these systems.

K2-44 (EPIC 201295312) was identified as hosting a planet candidate by Montet et al. (2015) and Doppler spectroscopy constrains its mass to be $<12 M_{\oplus}$ (95% confidence; Van Eylen et al. 2016a). Our analysis of this system yields FPP < 0.01 and thus validates this previously identified candidate.

Of the nine planet candidates identified by Montet et al. (2015), we validate five as planets: K2-44, K2-46, K2-8, K2-27, K2-35 (EPIC 201295312, 201403446, 201445392, 201546283, and 201549860, respectively). For three candidates (EPIC 201702477, 201617985, and 201565013), we find $0.01 <$ FPP < 0.99. For EPIC 201828749 we find FPP < 0.01, but a nearby star seen via high-resolution imaging prevents us from validating this candidate.

The largest single sample of *K2* planet candidates released to date is the 234 candidates identified by Vanderburg et al. (2016) in Campaigns 0–3. Our analysis independently identifies 127 of their candidates. Of these 127, we validate 72 as planets and identify 19 as false positives. Our analysis validates several multi-planet candidate systems announced in that work: K2-23, K2-58, K2-59, K2-62, K2-63, and K2-75 (EPIC 206103150, 206026904, 206027655, 206096602, 206101302, and 206348688, respectively).

Furthermore, our analysis identifies 69 new candidates not published in the sample of Vanderburg et al. (2016); these are mostly in Campaign 4; some are in earlier Campaigns. The two samples largely overlap, but each also contains many candidates identified by only a single team. The differences between the two samples (along with our non-detection of EPIC 206318379, noted above) suggest that multiple independent analyses are essential if many planet candidates are not to be missed.

When comparing our sample with that of Vanderburg et al. (2016), we find that the largest single systematic difference between them is that they report roughly 25% more candidates with $P < 5$ days. Our vetting checks suggest that most of these excess short-period planets are eclipsing binaries. In particular, our early-stage vetting procedures (described in Section 2.3) indicate that EPIC 201182911, 201270176, 201407812, 201488365, 201569483, 201649426, 202072965, 202086968, 202093020, 202843107, 203942067, 204649811, 205463986, and 206532093 are all likely false positives. Furthermore, high-resolution imaging of a random selection of four of their candidate systems revealed all four to have nearby multiple stars (EPIC 203099398, 203867512, 204057095, 204750116). While these newly detected stars do not prove that the systems are false positives, they will nonetheless complicate any effort to validate these candidates.

Aside from the apparent excess of short-period false positives in the Vanderburg et al. (2016) sample, we find no statistical differences between the properties of theirs and our candidate samples. Measurements of both pipelines' detection efficiencies could determine why each team has missed so many of the candidates detected by the other group. The implication for future surveys is that multiple independent pipelines may substantially increase the total survey completeness of independent, relatively low-budget survey programs.

Adams et al. (2016) report nine new candidates in Campaigns 0–5 with $P < 1$ days. Of their five new candidates in Campaigns 0–4, we identify and validate one: K2-85b (EPIC 210707130b), which hosts a small planet on a 16 hr period. Because our transit search did not extend to ultra-short orbital periods, we did not identify EPIC 202094740, 203533312, 210605073, or 210961508.

Schmitt et al. (2016) identify several dozen systems as likely eclipsing binaries (see their Table 1). Of these we identify four: EPIC 201324549 is a false positive, while EPIC 201626686, 204129699, and 206135267 remain candidate planets. Of their planet candidates we find three to have low FPPs EPIC 201920032, 206061524, and 206247743) and we validate five as planets (K2-55, K2-60, K2-67, K2-73, and K2-76, respectively, EPIC 205924614, 206038483, 206155547, 206245553, and 206432863). We did not identify their candidate EPIC 201516974 because of its 36.7-day orbital period.

8. CONCLUSION AND FINAL THOUGHTS

We have presented 104 validated planets discovered using *K2* photometry and supporting ground-based observations. Of these, 64 are planets validated here for the first time. Our analysis shows that *K2* has increased by 30% the number of small (1–4 $R_{\oplus}$) planets orbiting bright stars (J = 8–12 mag), as depicted in Figure 12. We report several new multi-planet systems, including the four-planet system K2-72 (EPIC 206209135); for all these systems we verify that the derived stellar parameters are consistent for each planet in each system. Our analysis finds 63 remaining planet candidates, which likely include a substantial number of planets waiting to be validated. In this work, we specifically utilize all our available follow-up data to assess the candidate systems. We claim to validate candidates only when no other plausible explanations are available; for example, many systems remain candidates because of nearby stars detected by our high-resolution imaging.

The size of our validated-planet sample demonstrates yet again the power of high-precision time-series photometry to discover large numbers of new planets, even when obtained from the wobbly platform of *K2*. Since *K2* represents a natural transition from the narrow-field, long-baseline *Kepler* mission to the nearly all-sky, mostly short-baseline *TESS* survey, the

results of our *K2* efforts bode well for the productivity of the upcoming *TESS* mission. The substantial numbers of intermediate-sized planets orbiting moderately bright stars discovered by our (and other) *K2* surveys (Figure 12) will be of considerable interest for future follow-up characterization via RV spectroscopy and *JWST* transit observations (e.g., Greene et al. 2016).

We searched the entire sample of *K2* targets without regard for the different criteria used to propose all these stars as targets for the *K2* mission. Thus, although the planet population we present is broadly consistent with the early candidate population discovered by *Kepler* (e.g., Borucki et al. 2011), our results should not be used to draw conclusions about the intrinsic frequency with which various types of planets occur around different stars. To do so, we are already investigating a full end-to-end measurement of our survey completeness as a function of planet and stellar properties. By doing so, we also hope to compare the quality of the various input catalogs and selection metrics used to pick *K2* targets.

Both *K2* and *TESS* offer the potential for exciting new demographic studies of planets and their host stars. *K2* observes a qualitatively different stellar population than *Kepler*, namely a much larger fraction of late-type stars (Huber et al. 2016). Stellar parameters for these late-type systems derived from photometry alone are relatively uncertain, and follow-up spectroscopy is underway to characterize these stars (Dressing et al., in prep; Martinez et al., in prep). In addition to the difference in median SpT, *K2* also surveys a much broader range of Galactic environments than was observed in the main *Kepler* mission. These two factors suggest that, once *K2*'s detection efficiency is improved and quantified, the mission's data could address new questions about the intrinsic frequency of planets around these different stellar populations.

At present, when comparing our planets and candidates with those identified by Vanderburg et al. (2016) we find only a partial overlap between the two samples. This result could imply significant, qualitative differences in vetting effectiveness and survey completeness, and suggests that the analysis of transit survey data by multiple teams is an essential component of any strategy to maximize the number of discoveries. As noted in Section 6, we estimate that our sample has an overall FPR of 15%–30% (depending on the FPR of candidates with additional nearby stars), with an indication that FPP increases for larger sizes and shorter periods.

We therefore re-emphasize that lists of *K2* candidates and/or validated planets are not currently suitable for the studies of planetary demographics that *Kepler* so successfully enabled (e.g., Howard et al. 2012; Mulders et al. 2015). The best path forward to enabling such studies would seem to include robust characterization of pipeline detection efficiency, as was done with *Kepler* (Petigura et al. 2013b; Dressing & Charbonneau 2015; Christiansen et al. 2015). It may be that such an approach, combined with further refinement of the existing photometry and transit detection pipelines, would allow the first characterization of the frequency of planet occurrence with Galactic environment across the diverse stellar populations probed by *K2*'s ecliptic survey.

Barring unexpected technical mishaps, *K2* is currently capable of operating through at least C18. The number of targets observed in these first *K2* campaigns contains comparable numbers of targets to later campaigns (with the exception of Campaign 0, which had a duration only roughly half that of the later, ~80 day campaigns). If *K2* continues to observe, based on current discoveries we would expect a planet yield roughly 4–5 times as great as that currently produced. Accounting for the relatively large survey incompleteness revealed by comparing our results to other *K2* surveys (Vanderburg et al. 2016), we expect *K2* to find anywhere from 500 to 1000 planets over its total mission lifetime. Analysis and follow-up of these systems will occupy exoplanet observers up to the *TESS* era, and beyond.

For useful suggestions and comments on an early draft we thank Andrew Vanderburg, Knicole Colon, Tim Morton, and Michael Werner. We thank Katherine de Kleer and Imke de Pater for contributing observations, and our many, many telescope operators and observing assistants for helping us obtain such a wealth of data.

This paper includes data collected by the *K2* mission. Funding for the *K2* mission is provided by the NASA Science Mission directorate.

This work was performed in part under contract with the Jet Propulsion Laboratory (JPL) funded by NASA through the Sagan Fellowship Program executed by the NASA Exoplanet Science Institute. E.A.P. acknowledges support by NASA through a Hubble Fellowship grant awarded by the Space Telescope Science Institute, which is operated by the Association of Universities for Research in Astronomy, Inc., for NASA, under contract NAS 5-26555. The Research of JES was supported by an appointment to the NASA Postdoctoral Program at the NASA Ames Research Center, administered by Universities Space Research Association under contract with NASA. B.J.F. was supported by the National Science Foundation Graduate Research Fellowship under grant No. 2014184874. Any opinion, findings, and conclusions or recommendations expressed in this material are those of the authors and do not necessarily reflect the views of the National Science Foundation. A.J. acknowledges support from FONDECYT project 1130857, BASAL CATA PFB-06, and from the Ministry for the Economy, Development, and Tourism's Programa Iniciativa Científica Milenio through grant IC 120009, awarded to the Millennium Institute of Astrophysics (MAS).

Some of the data presented herein were obtained at the W.M. Keck Observatory (which is operated as a scientific partnership among Caltech, UC, and NASA) and at the Infrared Telescope Facility (IRTF, operated by UH under NASA contract NNH14CK55B). The authors wish to recognize and acknowledge the very significant cultural role and reverence that the summit of Maunakea has always had within the indigenous Hawaiian community. We are most fortunate to have the opportunity to conduct observations from this mountain.

C.B. acknowledges support from the Alfred P. Sloan Foundation. The Robo-AO system was developed by the collaborating partner institutions, the California Institute of Technology and the Inter-University Centre for Astronomy and Astrophysics, and with the support of the National Science Foundation under grant Nos. AST-0906060, AST-0960343, and AST-1207891, the Mt. Cuba Astronomical Foundation, and by a gift from Samuel Oschin.

The Pan-STARRS1 Surveys (PS1) have been made possible through the contributions of the Institute for Astronomy, the University of Hawaii, the Pan-STARRS Project Office, the Max Planck Society and its participating institutes, the Max

Planck Institute for Astronomy, Heidelberg and the Max Planck Institute for Extraterrestrial Physics, Garching, The Johns Hopkins University, Durham University, the University of Edinburgh, Queen's University Belfast, the Harvard-Smithsonian Center for Astrophysics, the Las Cumbres Observatory Global Telescope Network Incorporated, the National Central University of Taiwan, the Space Telescope Science Institute, the National Aeronautics and Space Administration under grant No. NNX08AR22G issued through the Planetary Science Division of the NASA Science Mission Directorate, the National Science Foundation under grant No. AST-1238877, the University of Maryland, and Eotvos Lorand University (ELTE).

Facilities: APF (Levy), *Kepler*, *K2*, Keck:I (HIRES), Keck:II (NIRC2), IRTF (SpeX), Palomar:Hale (PALM-3000/PHARO), Palomar:1.5 m (Robo-AO), Gemini:North (DSSI), Gemini:South (NIRI), LBT (LMIRCam).

REFERENCES

Adams, E. R., Ciardi, D. R., Dupree, A. K., et al. 2012, AJ, 144, 42
Adams, E. R., Jackson, B., & Endl, M. 2016, AJ, 152, 47
Aller, K. M., Kraus, A. L., Liu, M. C., et al. 2013, ApJ, 773, 63
Almenara, J. M., Astudillo-Defru, N., Bonfils, X., et al. 2015, A&A, 581, L7
Angus, R., Foreman-Mackey, D., & Johnson, J. A. 2016, ApJ, 818, 109
Armstrong, D. J., Kirk, J., Lam, K. W. F., et al. 2016, MNRAS, 456, 2260
Armstrong, D. J., Santerne, A., Veras, D., et al. 2015, A&A, 582, A33
Baranec, C., Riddle, R., Law, N. M., et al. 2013, Journal of Visualized Experiments, 72, e50021
Baranec, C., Riddle, R., Law, N. M., et al. 2014, ApJL, 790, L8
Baranne, A., Mayor, M., & Poncet, J. L. 1979, VA, 23, 279
Barros, S. C. C., Almenara, J. M., Demangeon, O., et al. 2015, MNRAS, 454, 4267
Becker, J. C., Vanderburg, A., Adams, F. C., Rappaport, S. A., & Schwengeler, H. M. 2015, ApJL, 812, L18
Beichman, C., Livingston, J., Werner, M., et al. 2016, ApJ, 822, 39
Borucki, W. J., Koch, D. G., Basri, G., et al. 2011, ApJ, 736, 19
Boyajian, T. S., von Braun, K., van Belle, G., et al. 2012, ApJ, 757, 112
Christiansen, J. L., Clarke, B. D., Burke, C. J., et al. 2015, ApJ, 810, 95
Ciardi, D. R., Beichman, C. A., Horch, E. P., & Howell, S. B. 2015, ApJ, 805, 16
Coelho, P., Barbuy, B., Meléndez, J., Schiavon, R. P., & Castilho, B. V. 2005, A&A, 443, 735
Collier Cameron, A., Wilson, D. M., West, R. G., et al. 2007, MNRAS, 380, 1230
Coughlin, J. L., Mullally, F., Thompson, S. E., et al. 2016, ApJS, 224, 12
Crossfield, I. J. M., Petigura, E., Schlieder, J. E., et al. 2015, ApJ, 804, 10
Dai, F., Winn, J. N., Albrecht, S., et al. 2016, ApJ, 823, 115
David, T. J., Hillenbrand, L. A., Cody, A. M., Carpenter, J. M., & Howard, A. W. 2016a, ApJ, 816, 21
David, T. J., Hillenbrand, L. A., Petigura, E. A., et al. 2016b, Natur, 534, 658
Dekany, R., Roberts, J., Burruss, R., et al. 2013, ApJ, 776, 130
Díaz, R. F., Almenara, J. M., Santerne, A., et al. 2014, MNRAS, 441, 983
Dotter, A., Chaboyer, B., Jevremović, D., et al. 2008, ApJS, 178, 89
Dressing, C. D., & Charbonneau, D. 2015, ApJ, 807, 45
Espinoza, N., et al. 2016, arXiv:1601.07635
Feiden, G. A., & Chaboyer, B. 2012, ApJ, 757, 42
Foreman-Mackey, D., Hogg, D. W., Lang, D., & Goodman, J. 2012, arXiv:1202.3665
Foreman-Mackey, D., Montet, B. T., Hogg, D. W., et al. 2015, ApJ, 806, 215
Fulton, B. J., Howard, A. W., Winn, J. N., et al. 2013, ApJ, 772, 80
Greene, T. P., Line, M. R., Montero, C., et al. 2016, ApJ, 817, 17
Grziwa, S., Gandolfi, D., Csizmadia, S., et al. 2015, arXiv:1510.09149
Hayward, T. L., Brandl, B., Pirger, B., et al. 2001, PASP, 113, 105
Hellier, C., Anderson, D. R., Collier Cameron, A., et al. 2012, MNRAS, 426, 739
Hirano, T., Fukui, A., Mann, A. W., et al. 2016, ApJ, 820, 41
Hodapp, K.-W., Irwin, E. M., Yamada, H., et al. 2003, Proc. SPIE, 4841, 869
Horch, E. P., Howell, S. B., Everett, M. E., & Ciardi, D. R. 2012, AJ, 144, 165
Horch, E. P., Veillette, D. R., Baena Gallé, R., et al. 2009, AJ, 137, 5057
Howard, A. W., Marcy, G. W., Bryson, S. T., et al. 2012, ApJS, 201, 15
Howard, A. W., Marcy, G. W., Johnson, J. A., et al. 2010, Sci, 330, 653
Howell, S. B., Rowe, J. F., Bryson, S. T., et al. 2012, ApJ, 746, 123
Howell, S. B., Sobeck, C., Haas, M., et al. 2014, PASP, 126, 398
Huang, C. X., Hartman, J. D., Bakos, G. Á., et al. 2015, AJ, 150, 85
Huber, D., Bryson, S. T., Haas, M. R., et al. 2016, ApJS, 224, 2
Huber, D., Ireland, M. J., Bedding, T. R., et al. 2012, ApJ, 760, 32
Johnson, M. C., Gandolfi, D., Fridlund, M., et al. 2016, AJ, 151, 171
Jordán, A., Brahm, R., Bakos, G. Á., et al. 2014, AJ, 148, 29
Kaiser, N., Aussel, H., Burke, B. E., et al. 2002, Proc. SPIE, 4836, 154
Kaufer, A., & Pasquini, L. 1998, Proc. SPIE, 3355, 844
Kolbl, R., Marcy, G. W., Isaacson, H., & Howard, A. W. 2015, AJ, 149, 18
Kraus, A. L., & Hillenbrand, L. A. 2007, AJ, 134, 2340
Kreidberg, L. 2015, PASP, 127, 1161
LaCourse, D. M., Jek, K. J., Jacobs, T. L., et al. 2015, MNRAS, 452, 3561
Law, N. M., Morton, T., Baranec, C., et al. 2014, ApJ, 791, 35
Leisenring, J. M., Skrutskie, M. F., Hinz, P. M., et al. 2012, Proc. SPIE, 8446, 84464F
Lépine, S., & Shara, M. M. 2005, AJ, 129, 1483
Lillo-Box, J., Demangeon, O., Santerne, A., et al. 2016, arXiv:1601.07635
Lissauer, J. J., Marcy, G. W., Rowe, J. F., et al. 2012, ApJ, 750, 112
Maldonado, J., Affer, L., Micela, G., et al. 2015, A&A, 577, A132
Mann, A. W., Gaidos, E., Mace, G. N., et al. 2016, ApJ, 818, 46
Marigo, P., Girardi, L., Bressan, A., et al. 2008, A&A, 482, 883
Montet, B. T., Morton, T. D., Foreman-Mackey, D., et al. 2015, ApJ, 809, 25
Morton, T. D. 2012, ApJ, 761, 6
Morton, T. D. 2015, VESPA: False Positive Probabilities Calculator, Astrophysics Source Code Library, ascl:1503.011
Morton, T. D., Bryson, S. T., Coughlin, J. L., et al. 2016, ApJ, 822, 86
Mulders, G. D., Pascucci, I., & Apai, D. 2015, ApJ, 814, 130
Narita, N., Hirano, T., Fukui, A., et al. 2015, ApJ, 815, 47
Neveu-VanMalle, M., Queloz, D., Anderson, D. R., et al. 2016, A&A, 586, A93
Osborn, H. P., Armstrong, D. J., Brown, D. J. A., et al. 2016, MNRAS, 457, 2273
Parviainen, H., & Aigrain, S. 2015, MNRAS, 453, 3821
Pecaut, M. J., & Mamajek, E. E. 2013, ApJS, 208, 9
Petigura, E. A. 2015, arXiv:1510.03902
Petigura, E. A., Howard, A. W., & Marcy, G. W. 2013a, PNAS, 110, 19273
Petigura, E. A., Howard, A. W., Lopez, E. D., et al. 2016, ApJ, 818, 36
Petigura, E. A., Marcy, G. W., & Howard, A. W. 2013b, ApJ, 770, 69
Petigura, E. A., Schlieder, J. E., Crossfield, I. J. M., et al. 2015, ApJ, 811, 102
Queloz, D. 1995, in IAU Symp. 167, New Developments in Array Technology and Applications, ed. A. G. D. Philip, K. Janes, & A. R. Upgren, 221
Ricker, G. R., Winn, J. N., Vanderspek, R., et al. 2014, Proc. SPIE, 9143 20
Rodriguez, D. R., Zuckerman, B., Kastner, J. H., et al. 2013, ApJ, 774, 101
Rowe, J. F., Bryson, S. T., Marcy, G. W., et al. 2014, ApJ, 784, 45
Sanchis-Ojeda, R., Rappaport, S., Pallé, E., et al. 2015, ApJ, 812, 112
Santerne, A., Díaz, R. F., Almenara, J.-M., et al. 2015, MNRAS, 451, 2337
Santerne, A., Hébrard, G., Lillo-Box, J., et al. 2016a, ApJ, 824, 55
Santerne, A., Moutou, C., Tsantaki, M., et al. 2016b, A&A, 587, A64
Schlieder, J. E., Crossfield, I. J. M., Petigura, E. A., et al. 2016, ApJ, 818, 87
Schmitt, J. R., Tokovinin, A., Wang, J., et al. 2016, AJ, 151, 159
Sinukoff, E., Howard, A. W., Petigura, E., et al. 2016, ApJ, 827, 78
Stassun, K. G., Pepper, J. A., Paegert, M., De Lee, N., & Sanchis-Ojeda, R. 2014, arXiv:1410.6379
Ter Braak, C. J. F. 2006, Statistics and Computing, 16, 239
Teske, J. K., Everett, M. E., Hirsch, L., et al. 2015, AJ, 150, 144
Torres, G., Fischer, D. A., Sozzetti, A., et al. 2012, ApJ, 757, 161
Torres, G., Fressin, F., Batalha, N. M., et al. 2011, ApJ, 727, 24
Valenti, J. A., & Fischer, D. A. 2005, ApJS, 159, 141
Van Cleve, J. E., Howell, S. B., Smith, J. C., et al. 2016, PASP, 128, 075002
Van Eylen, V., Albrecht, S., Gandolfi, D., et al. 2016b, arXiv:1605.09180
Van Eylen, V., Nowak, G., Albrecht, S., et al. 2016a, ApJ, 820, 56
Vanderburg, A., & Johnson, J. A. 2014, PASP, 126, 948
Vanderburg, A., Latham, D. W., Buchhave, L. A., et al. 2016, ApJS, 222, 14
Vanderburg, A., Montet, B. T., Johnson, J. A., et al. 2015, ApJ, 800, 59
Vogt, S. S., Allen, S. L., Bigelow, B. C., et al. 1994, Proc. SPIE, 2198, 362
Zenteno, A., Forster, F., Rest, A., et al. 2015, ATel, 7664
Ziegler, C., Law, N. M., Morton, T., et al. 2016, arXiv:1605.03584